Synthesis and Characterization of Heterostructured Metallic Films with Precisely Controlled Architectures

by

Rohit Berlia

A Dissertation Presented in Partial Fulfillment
of the Requirements for the Degree
Doctor of Philosophy

Approved March 2021 by the
Graduate Supervisory Committee:

Jagannathan Rajagopalan, Chair
Karl Sieradzki
Pedro Peralta
Peter Crozier
Kiran Solanki

ARIZONA STATE UNIVERSITY

December 2021

ABSTRACT

The increasing demand for structural materials with superior mechanical properties has provided a strong impetus to the discovery of novel materials, and innovations in processing techniques to improve the properties of existing materials. Methods like severe plastic deformation (SPD) and surface mechanical attrition treatment (SMAT) have led to significant enhancement in the strength of traditional structural materials like Al and Fe based alloys via microstructural refinement. However, the nanocrystalline materials produced using these techniques exhibit poor ductility due to the lack of effective strain hardening mechanisms, and as a result the well-known strength-ductility trade-off persists. To overcome this trade-off, researchers have proposed the concept of heterostructured materials, which are composed of domains ranging in size from a few nanometers to several micrometers. Over the last two decades, there has been intense research on the development of new methods to synthesize heterostructured materials. However, none of these methods is capable of providing precise control over key microstructural parameters such as average grain size, grain morphology, and volume fraction and connectivity of coarse and fine grains. Due to the lack of microstructural control, the relationship between these parameters and the deformation behavior of heterostructured materials cannot be investigated systematically, and hence designing heterostructured materials with optimized properties is currently infeasible. This work aims to address this scientific and technological challenge and is composed of two distinct but interrelated parts. The first part concerns the development of a broadly applicable synthesis method to produce heterostructured metallic films with precisely defined architectures. This method exploits two forms of film growth (epitaxial and Volmer-Weber) to generate heterostructured metallic films. The second part investigates the effect of different microstructural parameters on the deformation behavior of heterostructured metallic films with the aim of elucidating their structure-property relationships. Towards this end, freestanding heterostructured Fe films with different architectures were fabricated and uniaxially deformed using MEMS stages. The results from these experiments are presented and their implications for the mechanical properties of heterostructured materials is discussed.

ACKNOWLEDGMENTS

I am forever indebted to my adviser, Prof. Jagannathan Rajagopalan, for his contribution to my professional and personal growth that I will carry for the years to come. I would also like to thank my committee members Prof. Karl Sieradzki, Prof. Pedro Peralta, Prof. Peter Crozier and Prof. Kiran Solanki for taking their time to evaluate my work and for their invaluable inputs towards my dissertation.

My sincere thanks to all the individuals who have directly or indirectly helped me to grow professionally and personally all these years at ASU. I thank my lab mates (Rohit Sarkar, Ehsan, Paul, Suhas, Santhosh, Ramanan) for all the support and help they provided over the years. I would like to gratefully acknowledge the research facilities and staff support that I availed at the Eyring Materials Center and Nanofab at Arizona State University. My research would not have been possible without the financial support from National Science Foundation (Grant # 1454109). Lastly, I would like to thank my family, fiancée and my friends who have made this journey pleasant and enriched my life through their encouragement and support.

TABLE OF CONTENTS

Page

LIST OF TABLES vi

LIST OF FIGURES vii

CHAPTER

1 INTRODUCTION 1

2 LITERATURE REVIEW 5

2.1 Nanocrystalline Metals/Alloys 5

2.2 Heterostructured Materials 8

2.3 Limitations and Current Challenges 13

3 EXPERIMENTAL TOOLS AND METHODS 15

3.1 Microfabrication Tools 15

3.1.1 Magnetron Sputtering Tool 15

3.1.2 Photolithography 17

3.1.3 Dry/Wet Etching 17

3.2 MEMS Tensile Testing Device 20

3.3 Microstructural Characterization 20

CHAPTER Page

4 SYNTHESIS OF HETEROSTRUCTURED METALLIC FILMS WITH PRECISELY DEFINED ARCHITECTURES DIRECTLY ON Si SUBSTRATES 22

4.1 Introduction 22

4.2 Experimental Method 23

4.3 Results and Discussions 25

4.4 Conclusions 35

5 SYNTHESIS OF HETEROSTRUCTURED METALLIC FILMS USING A BUFFER LAYER ON Si SUBSTRATES 36

5.1 Introduction 36

5.2 Experimental Method 37

5.3 Results and Discussions 37

5.4 Conclusions 43

6 FABRICATION OF MEMS TENSILE STAGE FOR TESTING FREESTANDING HETEROSTRUCTURED METALLIC FILMS 44

6.1 Introduction 44

6.2 Challenges Addressed During MEMS Stage Fabrication 44

6.3 Fabrication of MEMS Tensile Testing Stage 47

CHAPTER Page

6.4 Conclusions 51

7 MECHANICAL CHARACTERIZATION OF HETEROSTRUCTURED Fe FILMS 52

7.1 Introduction 52

7.2 Experimental Method 54

7.3 Results 55

7.3.1 Microstructural Characterization 58

7.3.2 Mechanical Behavior of Bimodal Fe Films 60

7.3.3 Deformation behavior and fracture of heterostructured films 63

7.4 Discussions 65

7.5 Conclusions 71

8 CONCLUSIONS 72

8.1 Summary of Research Findings 72

8.2 Future Work 73

REFERENCES 75

LIST OF TABLES

Table Page

1: List of Bimodal Fe Samples With Their Microstructural Parameters and Mechanical Properties. 57

LIST OF FIGURES

Figure Page

1: Hall-Petch Effect in BCC Steels. The Straight Lines Show Hall-Petch Relationship for Different Steels [3]. 2

2: Schematic of a NC Material With Large Fraction of Atoms Residing in the Grain Boundaries (White) [22]. 6

3: TEM Bright Field Image and Selected Area Diffraction Pattern of a NC Alloy [26]. 6

4: Normalized Yield Strength vs Normalized Uniform Tensile Strain Plot of Metals/Alloys With Different Microstructures. The Yield Strength and Tensile Strain Values of Each Metal Were Normalized With Respect to Yield Strength and Tensile Strain of Their CG Counterpart, Respectively [32]. 7

5: Engineering Stress–Strain Curves of Cu With Different Microstructures. Curve A: CG Cu (Low Strength, High Ductility); Curve B & C: Room Temperature Rolled Cu & Cryo-Milled Cu (High Strength, Low Ductility); Curve D: Cryo-Milled Cu Annealed at 180°C; Curve E: Cryo-Milled Cu Annealed at 200°C (Improved Ductility but Strength Decreased). This Produced a Bi-modal Microstructure Improved Ductility but Also Decreased Strength (Curve E) [35]. 9

6: Tensile Stress-Strain Curves of an Al Alloy With Bimodal Microstructure and Different Volume Fraction of Coarse and UFG Domains [41]. 10

7: (left) TEM Micrograph of Electrodeposited Ni Film That Shows Nanoscale Ni Domains Embedded Within Ni Matrix Crystal. (right) Tensile Stress–Strain Curves of Ni. Tensile Stress-Strain Curves of Ni With Different Grain Sizes Ranging From 27 μm to 18 nm Along With Nanodomained Ni Electrodeposited Sample [20]. 11

8: (left) Cross Sectional Image of Gradient NC Cu Prepared by Surface Attrition. (right) Tensile Stress-Strain Curves for a CG Cu (red), a Free-standing NC Foil Sample (black) and a Gradient Nanograined With Interior CG (GNG/CG) Cu Sample. Inset Shows the Tensile GNG/CG bar Samples Before and After Tension [13]. 12

9: (left) TEM Image of Ti With Heterogeneous Lamella Structure That Shows a Lamella of Recrystallized Grains in Between Two Lamellae of UFG. (right) Tensile Stress-Strain Curves of Heterogeneous Lamella Ti Compared With UFG Ti and CG Ti [44]. 13

10: (left) Orion 5 Sputter Deposition Tool Used to Synthesize Metallic Films. (right) Magnetron Sputtering Guns Having Copper Targets. Pictures Courtesy of AJA International. 16

11: Schematic of the RIE Chamber. The Reactive Gases are Used to Etch Metal Films. Picture Courtesy of Oxford Instruments. 18

12: Schematic Representation of the Two Step Bosch Process [46]. 19

13: Synthesis of Metallic Films With Multimodal Microstructures. (a) A Thin, Amorphous SiN_x Layer (10-20 nm) is Deposited On a SC Si Wafer Using Low Pressure Chemical Vapor Deposition (LPCVD). (b) Photolithography is Used to Define the Desired Multimodal Microstructural Design.

Figure Page

(c) SiN_x Layer is Etched Using Reactive Ion Etching (RIE) to Expose the Underlying Si Substrate at Specific Regions. (d) Photoresist is Removed Using a Photoresist Stripper. (e) The Wafer is Immersed in 49% HF Solution to Etch the Silicon Dioxide on the Wafer Surface. Exposure to HF Passivates the Si Surface With Hydrogen for 30-60 mins and Prevents it From Reoxidizing. (f) The Patterned Wafer is Transferred to a Sputtering Chamber Within 5-10 Minutes to Deposit the Metallic Film With Multimodal Microstructure........ 25

14: (a) θ-2θ XRD Scan of Epitaxially Grown 1 μm Thick Cu Film on Si(100) Substrate. (b) ϕ Scan Showing Cu(111) and Si(111) Reflections While Rotating the Wafer About [100] Axis. Note That the Intensity is in Logarithmic Scale. (c) Rocking Curve (ω Scan) of Cu(200) Peak. 26

15: (a, b) Bright Field TEM image of Cu Film With Bimodal Microstructure at Lower and Higher Magnifications. SADP of the Polycrystalline and Epitaxial Region is Shown as Inset in (a) and (b). 277

16: EBSD Maps of a 250 nm Thick Bimodal Cu Film Along Out-of-Plane Direction (a) and Along Two Mutually Perpendicular In-Plane Directions (b, c). The Color-Coded Orientation for the EBSD Maps in (a-c) is Shown in the Standard Triangle (Right, Lower Panel) Along With a Schematic That Shows a Si (100) Wafer Represented With the Directions and Pattern Shown on it. 28

17: Schematics of the Plan View of (a) Top Layer of Si (100) (b) Top Layer of Cu (100) (c) Cu (001) Layer Rotated by 45° Along [001] (d) Cu Atoms With Respect to the Si Atoms After Epitaxy is Formed. Si Atoms are Represented in Grey and Cu in Orange. 29

18: (a) θ-2θ XRD Scan of a 1.56 μm Thick Epitaxially Grown Fe Film on Si(111) Substrate. (b) ϕ Scan Showing Si(220) and Fe(220) Reflections as the Sample is Rotated About [111] Axis. Note That the Intensity is in Logarithmic Scale. (c) Rocking Curve of Fe(222) Peak. 30

19: ϕ Scans of 25 nm, 200 nm and 1.56 μm Thick Fe Films Showing Fe(220) Reflections While Rotating the Sample About the [111] Axis. The Higher Intensity Peaks Correspond to Twinned Epitaxy of Fe(111) on Si(111). Note That the Intensity is in Logarithmic Scale. 31

20: (a, b) Bright Field TEM Micrographs of a 175 nm Thick Fe Film With Bimodal Microstructure at Lower and Higher Magnifications. SADP of the Monocrystalline and Polycrystalline Region is Shown as Inset in (a) and (b). 32

21: (a-f) EBSD Maps of a 175 nm Thick Fe Film Along Out-of-Plane Direction (a) and Along Two Mutually Perpendicular In-Plane Directions (b, c). The Film is Composed of Three Distinct Regions – the SC Matrix, the NC Rings and Monocrystalline Circular Regions Enclosed by the Rings. (d-f) EBSD Maps of a 175 nm Thick Fe Film With a NC Matrix Punctuated by Monocrystalline Ring Structures. The Color-Coded Orientation for the EBSD Maps in (a-f) is Shown in the Standard Triangle Along With a Schematic That Shows a Si (111) Wafer Represented With the Directions and Pattern Shown on it. 33

22: Schematics of (a) Si(111) Plane. The Possible Locations of Si Atoms in (111) Planes (A, B, C) Are Shown. (b) Fe(111) Plane. (c) Aligned Epitaxy of Fe(111) on Si(111), Which Preserves the ABCABC Stacking Order. (d) Twinned Epitaxy of Fe(111) on Si(111), Which Leads to ABCBAC Stacking. 34

Figure Page

23: (a) θ-2θ Scan of 200 nm Epitaxial Cr Grown on 20 nm Fe/Si Substrate (b) ϕ Scan of Si (220) (above) and Fe (220) (below) Reflections While Rotating the Sample About [111] Axis (c) ω-Scan of Cr (111) Peak 38

24: EBSD Micrographs of a Heterostructured Cr Film Deposited on a Patterned Si/Fe Substrate (a) Along A3, (b) Along A2 and (c) Along A1. Schematic Shows a Si (111) Wafer Represented with the Directions Shown on it. Color Representation for Each Orientation is Shown in the Standard Triangle. 39

25: Schematic Representation of Each Step Involved in the Synthesis of Heterostructured Ni Film Through Microfabrication Processes. 40

26: EBSD Micrographs of a Heterostructured Ni Film Deposited on a Patterned Ag/Si Substrate (a) Along A3, (b) Along A2 and (c) Along A1. The Microstructure Contains a Parallel Arrangement of NC and Epitaxial Regions. Schematic Shows a Si (001) Wafer Represented With the Directions Shown on it. Color Representation for Each Orientation is Shown in the Standard Triangle. 41

27: EBSD Micrographs of a Heterostructured Ni Film Deposited on a Patterned Ag/Si Substrate (a) Along A3, (b) Along A2 and (c) Along A1. The Microstructure Contains NC Domains Within an Epitaxial Matrix. Schematic Shows a Si (001) Wafer Represented With the Directions Shown on it. Color Representation for Each Orientation is Shown in the Standard Triangle. 42

28: Variation of Residual Stress With (left) Ar Pressure With Substrate Kept at Zero Potential (right) Bias Voltage Between -15 V and -165 V With Constant Deposition Pressure at 0.266 Pa [85]. .. 46

29: (a) A Heterostructured Fe Film Deposited on a Wafer by Magnetron Sputtering. (b) The Wafer Was Spin Coated With Photoresist on the Front and Backside. 48

30: (a) Photoresist Patterned on the Front and Backside by Exposure to UV Light Followed by Photoresist Development. (b) The Pattern is Transferred to Metal Layer by Etching Fe Using Dilute Nitric Acid. 49

31: (a) Anisotropic Etching of Si Using Si Deep Etcher From the Back all the Way to the Top. (b) Photoresist Removal From the Top and Bottom. 49

32: Optical Image of a MEMS Tensile Testing Stage With a Co-fabricated, Freestanding Metal Sample With a Bimodal Microstructure. The Sample and Gauges (G1, G2 and G3) are Shown at Higher Magnification in the Bottom Figure. An Enlarged View of a Part of the Sample is Shown in the Inset. The Darker Regions in the Inset are SCs Whereas the Lighter Regions are Polycrystals. 50

33: Schematic of Fe Films with Different Bimodal Architectures That Were Synthesized and Tested. The Purple Color Corresponds to SC Domains While Yellow Color Corresponds to NC Domains. W_{SC} and W_{NC} are the Widths of the SC and NC Domains. 56

34: (a-c) EBSD Maps of a Bimodal PA Film Sample. The Colors Correspond to Crystal Orientation (See Standard Triangle in (f)) With Respect to the Out-of-Plane Direction (a) and Two In-Plane Directions (b and c). (d, e) EBSD Maps of a SA Sample and WA Sample Showing Their Out of-Plane Orientation. (f) Schematic of a Si (111) Wafer Showing $[11\bar{1}]$, $[1\bar{1}0]$ and [112] Directions. An

Figure Page

Image of the MEMS Stage is Superimposed to Show its Orientation With Respect to the Si Wafer....59

35: Bright Field TEM Micrograph of a 175 nm Thick Bimodal PA Sample. SADP of the SC and NC Domain are Shown as Insets in (a) and (c). 59

36: Stress-Strain Response of (a) Pure SC and NC Fe Film, and (b) Bimodal PA Samples With Different Volume Fractions of NC Domains. 60

37: Stress – Strain Curves of (a) PA, (b) SA and (c) WA Samples With Different W_{SC} and Equal (50%) Volume Fractions of NC and SC Domains. 62

38: Stress – Strain Curves of Bimodal Samples With Different Architectures but Equal Volume Fractions of SC and NC Domains. 62

39: Deformed Microstructure of a (a) PA, (b) SA and (c) WA Sample. Slip Bands With (110) Traces are Clearly Visible Within the SC Domains. 64

40: SEM Micrographs of a Fractured (a) PA, (b) SA and (c) WA Sample. In the PA Sample, the Region Outside the Red Dashed Lines Correspond to the Sample Top Surface Whereas the Region Within the Red Dashed Lines Correspond to the Fracture Surface. The SA Sample Fractured at an Angle of 45° to the Loading Direction Near the Edge and Perpendicular to the Loading Direction in the Middle. The WA Sample Showed a Tendency to Localize Slip Along Adjacent SC Domains Oriented in the Same Direction. Two Sets of Such SC Domains are Outlined in (c). 65

41: Schematic Illustration of Possible Dislocation Glide Planes, (101) and (011), for SC Fe Deformed Along [112]. The Burgers Vector of the Dislocations in These Planes are Also Shown. 66

42: Schematic of Dislocation Pile-Ups in WA Samples with Different W_{SC}. The Number of Dislocations in the Pile-Ups Does Not Increase Significantly With W_{SC} But the Distance Between the Pile-Ups (δ) Does. 68

43: Schematic of Dislocation Pile-Ups That Occurs Within SC Domains of PA, SA, WA Samples with Different W_{SC}. 69

CHAPTER 1

INTRODUCTION

The motivation behind this thesis is to develop a method to generate heterostructured metallic films with precisely controlled architectures that can enable us to study the effect of various microstructural parameters on the deformation behavior of these films. With the increasing demand of materials with superior mechanical properties, there is a need of structural materials that possess higher strength and toughness. Since the discovery of copper (around 9000 BC), humans have strived continuously to discover new metals/alloys/techniques to fulfil their technological needs. The advancements in the field of alloy development and manufacturing have led to significant evolution in the field of metallurgy. The quest for discovering new alloys like high entropy alloys and the search of new processing techniques like severe plastic deformation to improve the properties of existing materials continues. Over the last few decades, severe plastic deformation techniques have led to a significant achievements in the field materials processing by enabling production of bulk nanocrystalline (NC) or ultrafine grain (UFG) materials [1,2].

NC metals/alloys are materials with average grain sizes less than 100 nm. They show promising mechanical properties where the strength increases by an order of magnitude when compared to their coarse-grained (CG) counterparts (grain size > 1 μm) as shown in Fig. 1 [3]. The strength in NC materials increase due to the reduction in grain size and the presence of high-volume fraction of grain boundaries (could be as high as 50%). This is very well known as the “Hall-Petch relationship” which predicts the relationship of strength to be inversely proportional to the square root of the grain size [4]. Due to the presence of very small grain size, multiple mechanisms like lattice dislocation slip, nucleation and movement of partial dislocation, twin formation, grain boundary sliding and diffusion operate in NC microstructures and leads to large increase in strength [5]. In addition, NC materials also exhibit other attractive properties such as excellent fatigue and wear resistance, increased diffusivity, higher thermal expansion coefficient, enhanced specific heat, lower thermal conductivity, and better soft magnetic properties. Unfortunately, due to lack of

strain hardening ability in these microstructures, they tend to fracture at very low strain (< 5%). If a material has such low strain to failure, it can lead to catastrophic failure of a component during service.

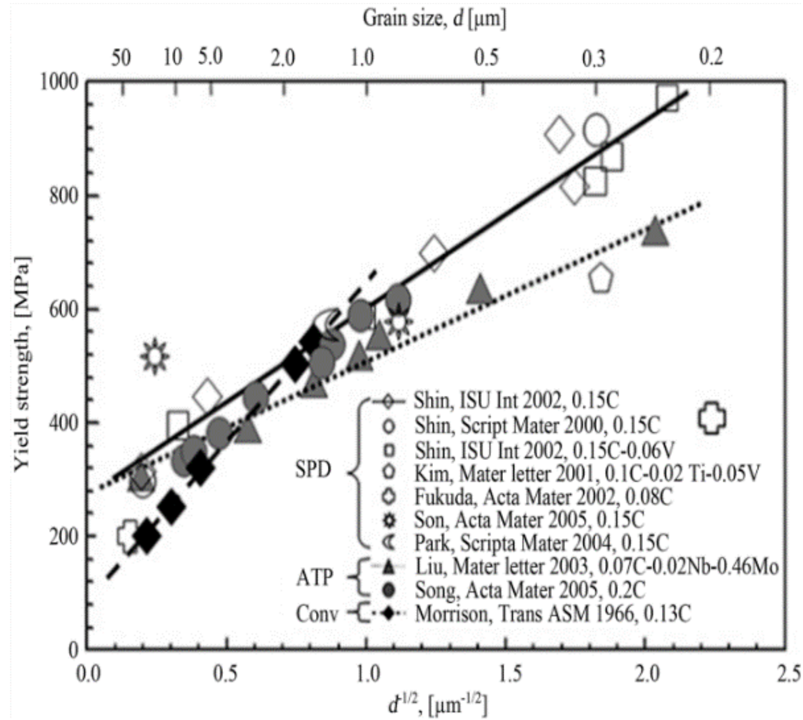

Figure 1: Hall-Petch effect in BCC steels. The straight lines show Hall-Petch relationship for different steels [3].

The reduction in grain size, leading to the increase in strength, is the very reason for the loss of strain hardening ability. The dislocations that nucleate at a grain boundary travel across the grain and is annihilated at the opposite grain boundary, resulting in no accumulation or storage of the dislocations in the interior of the grains [6–8]. The increase of strength at the expense of ductility is a well-known phenomenon commonly known as “strength-ductility trade-off”. Extensive research is still being conducted to generate metals/alloys with a combination of superior strength and toughness. One promising approach to optimize the strength and ductility is by generating heterostructured materials [9,10].

Heterostructured materials consist of microstructure that has considerable variation in either the size, orientation, or phase composition of the grains. For example, heterostructured materials are often composed of grains that vary in size from tens of nanometers to tens of micrometers. The role of smaller grains is to provide strength and that of the larger grains is to enable strain hardening through dislocation accumulation and storage. Various techniques/strategies have been explored to generate heterostructured materials to overcome the strength-ductility trade-off [11,12]. Surface treatments were typically used to produce a gradient microstructure in metallic sheets, with nanostructured grains near the surface and coarse grains in the middle [13,14]. Another common method to synthesize heterostructured metals involves ball milling to produce powders with nanometer and micrometer grain sizes and consolidating them [15–19]. In addition to these methods, pulsed electrodeposition can be used to produced nanodomains with small misorientations in UFG Ni matrix, which results in ultra-high strength and ductility [20]. However, few currently available techniques can produce heterostructured materials with good repeatability. More importantly, it is currently infeasible to precisely control microstructural parameters like the volume fraction of coarse and fine domains, grain size distribution, grain morphology, spatial arrangement, etc. Due to the lack of control on the microstructural parameters, very little is known about the influence of these parameters on the deformation behavior of heterostructured materials. For example, how would a material deform if it has different spatial arrangements of large grains - isolated versus connected – but the same volume fraction? Therefore, there is a need to develop a method that enables precise control of architectures to fine tune the desired mechanical properties.

The method developed in this thesis work involves the use of microfabrication techniques, like photolithography and dry etching. The key idea is to utilize the two different types of film growth simultaneously. When metallic films are grown on amorphous substrates via physical vapor deposition (PVD) processes such as sputtering, the films grow in a polycrystalline manner. In contrast, metal films deposited on crystalline substrates can grow with a specific orientation

relationship to the underlying substrate. This mode of growth, referred to as epitaxial growth, can be used to generate single crystal (SC) films when the substrate is also monocrystalline. Using this approach, heterostructured metallic films like Fe, Cu, Al, Ni, Ag and Cr were deposited and characterized. In addition, the mechanical characterization was performed through uniaxial mechanical testing on heterostructured Fe films using MEMS tensile testing stage.

In chapter 4 and chapter 5, two different methods are discussed in detail on how to synthesize heterostructured metallic films for multiple systems. A step-by-step methodology is discussed along with microstructural characterization of the films. The microstructural characterization of the films was performed using X-ray diffraction (XRD), electron backscattered diffraction (EBSD) and transmission electron microscopy (TEM). It also further elaborates on how this method can be used for other material systems that does not grow epitaxially on Si.

In chapter 6, the fabrication of MEMS tensile testing stage with the freestanding heterostructured Fe film is discussed. The initial challenges related to the residual stress development, clean patterning of Fe layer by wet etch method and the modifications involved in the MEMS stage to test thicker films are addressed. A detailed, step-by-step process involved in the fabrication of MEMS stage is described along with its working principle.

In chapter 7, the mechanical behavior of heterostructured Fe films with different architectures is discussed. A schematic of different sample architectures on which mechanical tests were performed is shown. Three different architectures were studied – parallel architecture (PA), series architecture (SA) and wave-like architecture (WA). The stress-strain responses of each heterostructured Fe film and their possible deformation mechanisms are discussed. The operative deformation mechanisms are interpreted from the scanning electron microscopy (SEM) images of the deformed samples.

Finally, in chapter 8, the research findings from this thesis work are summarized and potential future directions are discussed.

CHAPTER 2

LITERATURE REVIEW

2.1 Nanocrystalline Metals/Alloys

NC metals/alloys can be synthesized using top-down or bottom-up approach [21]. In top-down approach, nanostructures are formed by breaking down the microstructure in a bulk material. In contrast, in the bottom-up approach nanostructures are created by arranging atom-by-atom, layer-by-layer. The methods that belong to top-down approach are severe plastic deformation, cryo-milling and mechanical alloying. Bottom-up approaches include sputtering, CVD, electrodeposition, etc. A few methods that are very commonly employed to synthesize bulk NC materials are ball milling and consolidation, electrodeposition, and severe plastic deformation (SPD).

NC metals/alloys possess high volume fraction of grain boundaries (30% for 10 nm grains) compared to their conventional (CG) counterparts as shown in Fig. 2 and Fig. 3. Therefore, their properties are largely influenced by grain boundaries. For example, the elastic modulus was observed to decrease by 30% in these materials due to presence of high-volume fraction of grain boundaries, which are less ordered and densely packed than the grain interiors, and hence show larger compliance [5,22]. NC materials exhibit high yield strength/hardness, fracture strength, lower elongation and toughness, enhanced diffusivity, higher specific heat, enhanced thermal expansion coefficient, superior wear resistance, and enhanced super plasticity at lower temperatures and faster strain rates [23]. The strength of NC materials could be an order of magnitude higher than that of CG materials. Two deformation mechanisms that become prominent in NC metals are grain boundary sliding and emission of partial dislocations [24]. Interestingly, at grain size < 10 nm the Hall-Petch relationship breaks down because dislocation pileups are energetically unfavorable at these small length scales [25].

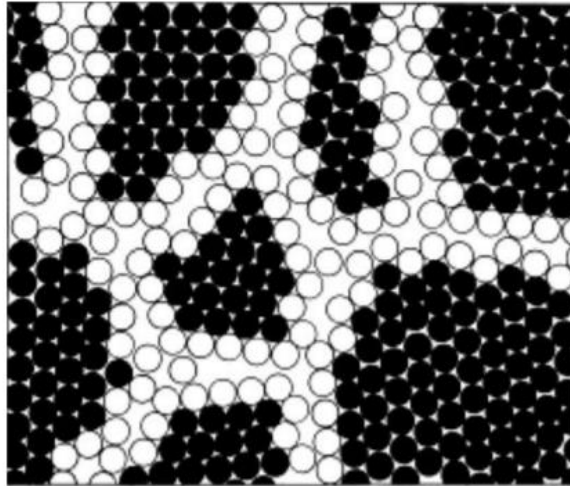

Figure 2: Schematic of a NC material with large fraction of atoms residing in the grain boundaries (white) [22].

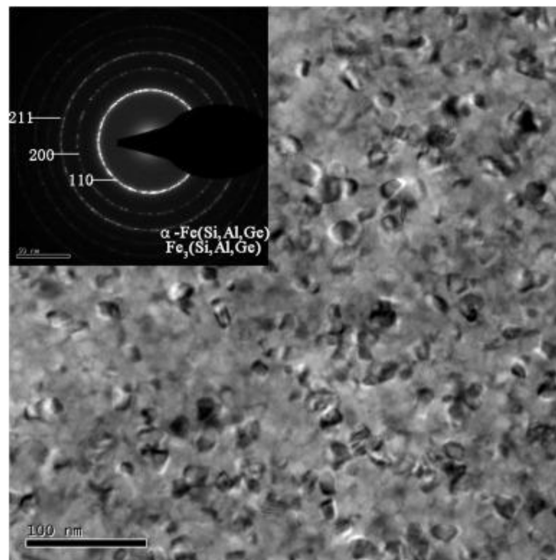

Figure 3: TEM bright field image and selected area diffraction pattern of a NC alloy [26].

Despite their superior properties like high strength and hardness, a major limitation of NC metals is their poor ductility, which has hindered their application as structural materials [27]. A concerted effort has been made to increase the ductility in these materials through several different

routes [28]. The two major reasons for lower ductility of NC metals are flaws or defects generated during processing and an intrinsic lack of strain hardening ability. The presence of defects like porosity and inclusion of unwanted elements like oxygen and nitrogen, which are detrimental during service, lead to formation of cracks and, thus, early failure [29,30]. On the other hand, lower strain hardening rate is attributed to the lack of dislocation accumulation and storage due to the very small grain sizes. According to the Hart Criterion, localized deformation will occur when $\gamma \leq 1\text{-}m$; where γ is the normalized strain hardening rate and m is the strain rate sensitivity [31]. Here, the effect of strain rate sensitivity is marginal to delaying the onset of localized deformation since most metals have small values of m at ambient temperatures. Therefore, several methods have been employed to synthesize heterostructured materials, which have significantly higher γ, to enhance the ductility in NC materials, as shown in Fig. 4. Such methods and their limitations are elaborated in the next two sections.

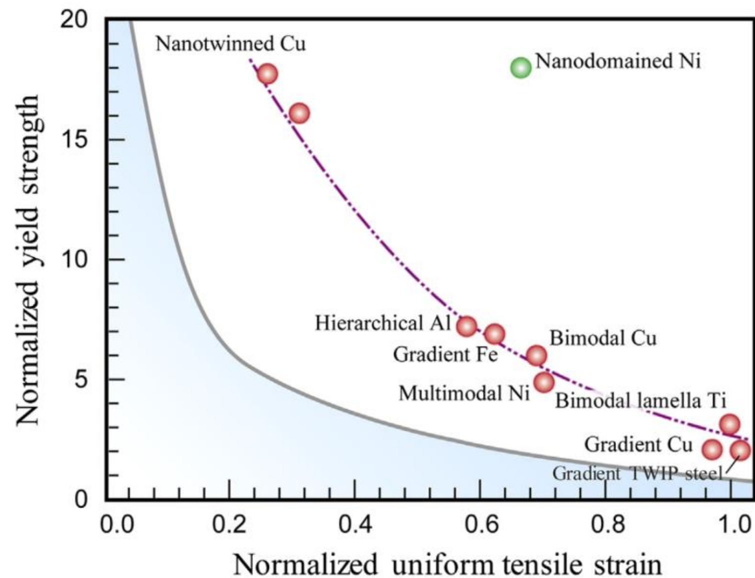

Figure 4: Normalized yield strength vs normalized uniform tensile strain plot of metals/alloys with different microstructures. The yield strength and tensile strain values of each metal were normalized with respect to yield strength and tensile strain of their CG counterpart, respectively [32].

2.2 Heterostructured Materials

Heterostructured materials are typically composed of domains with contrasting properties, e.g., plastically soft and hard domains. The heterogeneity in properties can arise due to microstructural heterogeneity, crystal structure heterogeneity or compositional heterogeneity and the domain sizes may vary from nanometers to millimeters. In heterostructured bulk materials, plastically hard domains yield at higher stress whereas plastically soft domains show higher strain hardening capability. The synergistic interaction between these domains lead to a superior combination of strength and ductility in heterostructured materials. Initially, the soft (large grains) and hard domains (small grains) deform elastically, which is followed by dislocation slip in soft domains that have smaller yield strength. Even as dislocation slip initiates in soft domains, the hard domains continue to deform elastically. To maintain strain compatibility at the interface between the soft and hard domains, geometrically necessary dislocations are introduced in the soft domains that increases the overall strength of the material. Once hard domains start to deform plastically, more strain is accommodated within soft grains leading to strain partitioning that produces back stress work hardening [33]. The above explained deformation mechanism also holds good for materials with varying strength within a microstructure [34]. Some of the methods to produce heterostructured materials are discussed below.

Ma and co-workers [35] performed one of the key experiments that showed a combination of high strength and tensile ductility was possible in heterostructured copper (Fig. 5). The samples were initially cryo-rolled to >90% strains to obtain high dislocation density and avoid dynamic recovery, followed by short annealing (3 minutes) at 200°C. The cryo-rolling introduced nanostructured phases and the annealing process led to abnormal recrystallization, overall resulting in the generation of bimodal microstructure with micron sized (1-3 μm) and nano-sized grains. The yield strength increased to 340 MPa, i.e., seven times that of the CG Cu, with uniform elongation of 30%. The superior mechanical properties of the bimodal microstructure helped motivate the synthesis of variety of heterostructured materials.

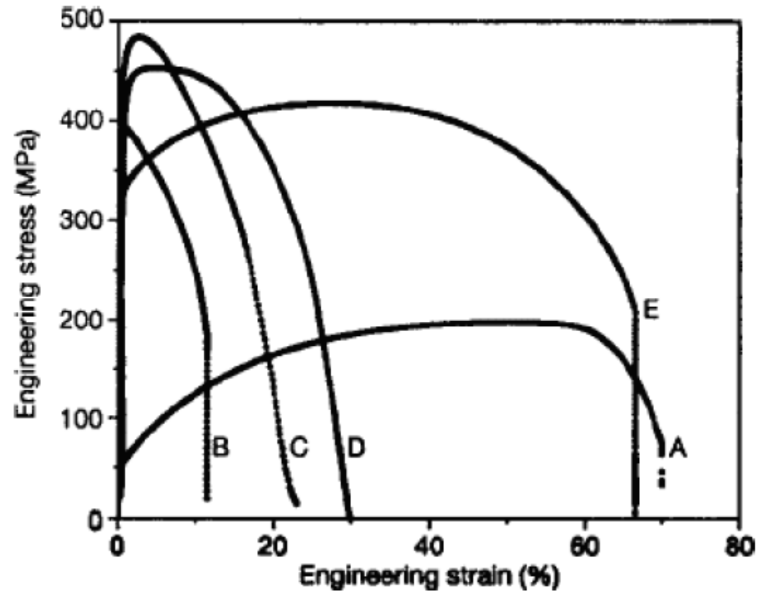

Figure 5: Engineering stress–strain curves of Cu with different microstructures. Curve A: CG Cu (low strength, high ductility); curve B & C: room temperature rolled Cu & cryo-milled Cu (high strength, low ductility); curve D: cryo-milled Cu annealed at 180°C; curve E: cryo-milled Cu annealed at 200°C (improved ductility but strength decreased). This produced a bi-modal microstructure improved ductility but also decreased strength (curve E) [35].

Another well-known method for producing heterostructured metals involves ball milling of different sized particles (nm to microns range), which are then consolidated to obtain materials with a microstructure with wide grain size distribution. This method has proven to be a simple way to obtain heterostructured materials with optimal strength-ductility combination [10,15]. During the initial development of ball milling and consolidation process to develop heterostructured materials, problems arising from processing, mainly porosity, led to early fracture of the samples [17,36]. Even after achieving theoretical density, the weaker bonding between the particles due to the surfactants used lead to embrittlement. Nevertheless, work on Al-alloys from Lavernia and co-workers [37–39] showed enhanced properties, as shown in Fig. 6. In their work, Al-alloy was ball milled at liquid nitrogen temperatures followed by powder compaction by hot isostatic pressing and extrusion. In

Al 5083 alloys, around 200 nm grain size was achieved in NC regions and some large grains (micron sized) were obtained from mixing cryo-milled and un-milled powders [40]. The variation in the volume fraction of combination of large and NC grains affected the stress – strain curves correspondingly. Similarly, in Al - 7.5% Mg alloy, the larger grains were incorporated through addition of un-milled alloy powders of micron size to the existing cryo-milled NC alloy powders [41]. The ratio of volume fraction of cryo-milled to un-milled powders (larger grains) showed the change in strength and ductility by enabling strain hardening within larger grains and strengthening by smaller grains.

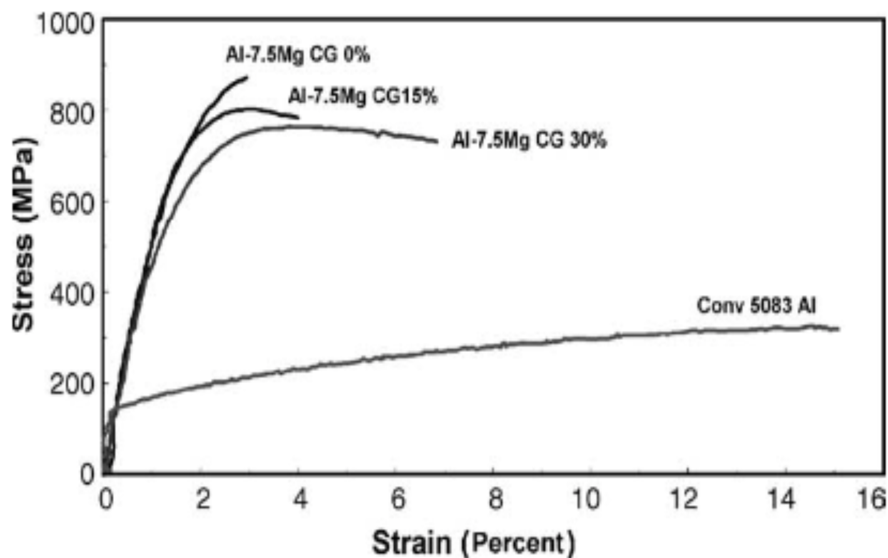

Figure 6: Tensile stress-strain curves of an Al alloy with bimodal microstructure and different volume fraction of coarse and UFG domains [41].

Using pulsed electrodeposition method, nanodomained Ni, as shown in Fig. 7, was produced that contains a UFG matrix with 200 nm mean grain size. These ultrafine Ni grains were embedded with 8 nm sized Ni domains [20]. Despite the volume fraction of these nanodomain Ni being only 2 vol %, the resulting material has yield strength of 1.3 GPa (comparable to NC Ni with uniform grains) and uniform elongation of 30% (comparable to CG metal). The outstanding

strengthening in this material is achieved due to the blockage of dislocations by the nanoscale domains which act like precipitates in precipitation hardened alloys. The nanoscale Ni domains also enable dislocation multiplication while providing sufficient space within the grain for dislocations to entangle and accumulate during deformation.

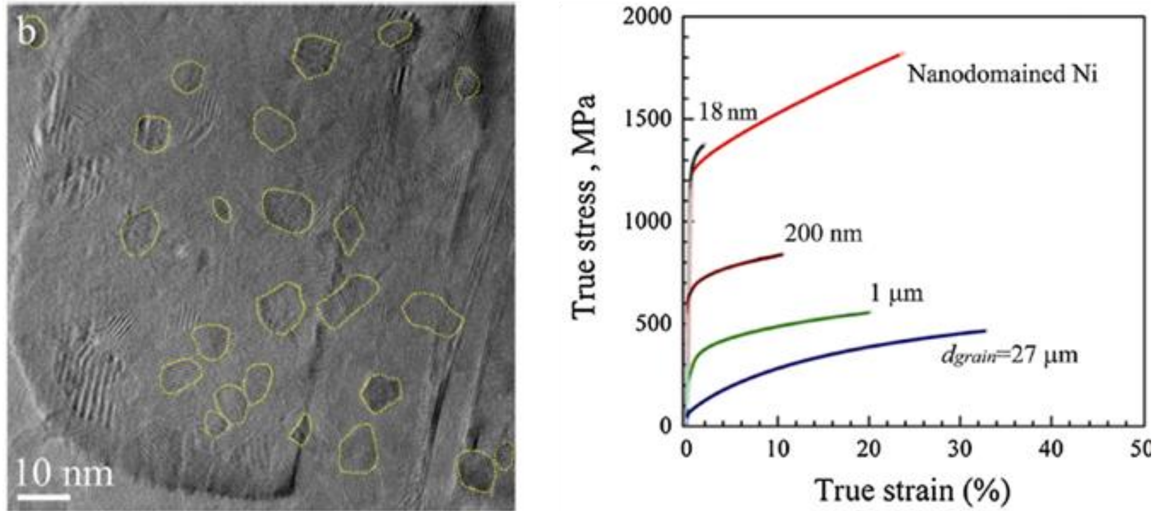

Figure 7: (left) TEM micrograph of electrodeposited Ni film that shows nanoscale Ni domains embedded within Ni matrix crystal. (right) Tensile stress–strain curves of Ni. Tensile stress-strain curves of Ni with different grain sizes ranging from 27 µm to 18 nm along with nanodomained Ni electrodeposited sample [20].

Surface mechanical attrition treatment (SMAT) and surface mechanical griding treatment (SMGT) are the methods used to generate gradient NC materials [42,43]. This technique enables the generation of nanostructures on the surface of a bulk CG metals. In SMAT, steel balls are vibrated at ultrasonic frequencies and impacted on the sample surface over a short time. In SMGT, a sample is grinded against a hard carbide tip to produce severe plastic deformation at the surface as shown in Fig. 8. In both the cases, the surface layers are severely deformed to produce nanoscale microstructures. Fang et al. used SMGT to produce a gradient microstructure consisting of nanograins on the surface (mean grain size 20 nm), up to a depth of 60 µm, UFG (mean grain

size 300 nm) in the transition region of 60 μm - 150 μm, and CG (μm scale) in the center [13]. The sample showed significant increase in strength and over 100% true strain in tension. Similar mechanical behavior was observed in samples prepared by SMAT. The reason for higher strain hardening behavior in these samples was the build-up of geometrically necessary dislocations and role of multiaxial axial stress state from different phases in activation of new slip systems and dislocation storage.

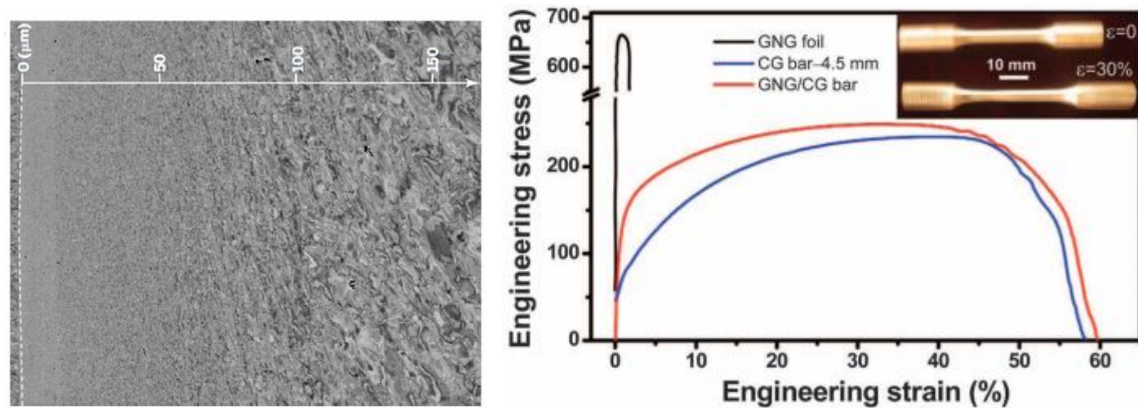

Figure 8: (left) Cross sectional image of gradient NC Cu prepared by surface attrition. (right) Tensile stress-strain curves for a CG Cu (red), a free-standing NC foil sample (black) and a gradient nanograined with interior CG (GNG/CG) Cu sample. Inset shows the tensile GNG/CG bar samples before and after tension [13].

Recently, heterostructured materials with harmonic structure and heterogeneous lamella structure, which have continuous three-dimensional networks of soft and hard domains, have been fabricated. Ameyama and co-workers synthesized harmonic structures of Cu which showed higher strength and ductility than bimodal microstructure Cu counterparts [18]. Interestingly, the ductility in these samples surpassed CG Cu samples at 19% UFG volume fraction. Wu et al fabricated heterogeneous lamella in Ti where network of soft coarse grains lamellae is embedded in the matrix of hard UFG lamella matrix as shown in Fig. 9. These samples were as strong as UFG Ti and as ductile as conventional CG Ti [44]. In this case, the extra hardening was attributed to the buildup

of geometrically necessary dislocations against the interface between soft and hard domains that create a back stress on the dislocations around it leading to further strengthening.

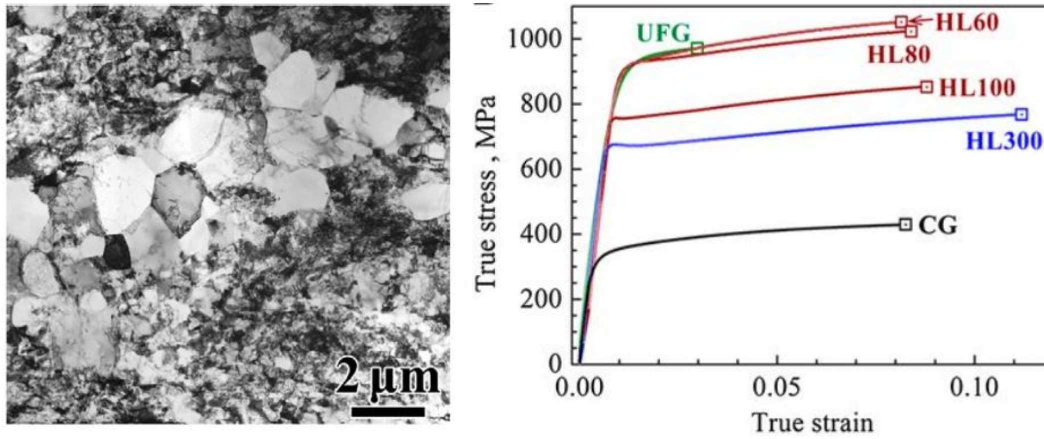

Figure 9: (left) TEM image of Ti with heterogeneous lamella structure that shows a lamella of recrystallized grains in between two lamellae of UFG. (right) Tensile stress-strain curves of heterogeneous lamella Ti compared with UFG Ti and CG Ti [44].

2.3 Limitations and Current Challenges

The research conducted so far demonstrates that heterostructured materials provide a clear path to achieve higher strength and ductility in metallic systems. However, the processing methods available today still faces challenges such as incorporation of impurities during processing, lack of reproducibility, and inability to control microstructural parameters. For example, during ball milling, the metal powders absorb impurities like Fe from steel ball, and C and N from binders that form carbide and nitride intermetallics, which act as potential sources of crack nucleation and propagation. Besides impurities, achieving 100% density through consolidation is a challenge resulting in porosities in the sample. The presence of porosity is detrimental to achieving higher ductility. In electrodeposition, additives act as grain refiners to achieve nanosized grains by increasing grain nucleation sites. Impurities like sulfur, which are present in the additives, accumulate in the grain boundaries and lead to early failure of the samples [28].

Another limitation of current processing techniques is the inability to reproducibly synthesize specific microstructures [32]. Since the mechanical properties are directly related to a microstructure, the lack of reproducibility can result in large scatter of the strength and ductility values. For example, it is extremely difficult to reproduce the volume fraction of fine and coarse domains and their exact grain size distribution using plastic deformation followed by annealing.

In addition, current methods do not allow control of key microstructural parameters like grain size distribution, spatial distribution of fine and coarse grains, and grain morphology even though they might provide control over certain parameters such as the volume fraction of coarse and fine grains. For instance, volume fraction of small grains and coarse grains can be controlled by using different powder sizes during consolidation, but their spatial location or morphology cannot be controlled. Similarly, SMAT or SMGT can create nanograined layers only to a depth of a few hundreds of microns [45]. The field of heterostructured metals would take a significant leap if such microstructures can be synthesized with robust control and repeatability. That would enable the researchers to understand the effect of each microstructural parameter on the mechanical behavior independently and eventually design the materials with required mechanical properties.

To summarize, there have been major advances in synthesizing and characterizing heterostructured metals and alloys. However, there are still several outstanding challenges that need to be overcome. Foremost among them is the capability to precisely control key microstructural parameters such as size, volume fraction and connectivity of coarse and fine grains, simultaneously and independently. This is essential to understand their effect on the mechanical properties, which is the first step towards designing heterostructured materials with optimized properties. This thesis addresses this key challenge and opens the possibility of creating functional materials with tailored morphologies and microstructures.

CHAPTER 3

EXPERIMENTAL TOOLS AND METHODS

This chapter details the major tools and techniques that were used to synthesize the heterostructured metallic films and MEMS tensile testing stage. This chapter is divided into two sections. The first section describes the tools that were used for microfabrication. The second section describes the tools that were used for microstructural characterization of heterostructured films.

3.1 Microfabrication Tools

Heterostructured metallic films and MEMS tensile testing stage were fabricated using microfabrication techniques that involve deposition, photolithography, dry/wet etching, and deep reactive ion etching. The tools and the methods employed used for each of these processes are explained below.

3.1.1 Magnetron Sputtering Tool

A magnetron sputtering system (Orion 5 system manufactured by AJA International) as shown in Fig. 10 was used to deposit the metallic films studied in this thesis. Sputtering is a physical vapor deposition method where inert gas (typically Ar) ions bombard the metallic target and sputters off atoms which get deposited on the substrate. It is a widely used technique that has the capability to deposit thin films with 2-3% thickness uniformity across a 4” wafer. It is well equipped to provide a good control on film thickness and composition. The Orion 5 sputtering tool has five confocal magnetron sputtering guns that can be used to sputter single component or multicomponent material systems. The tool possesses three DC and two RF power sources. The DC power sources are highly efficient in depositing metallic materials whereas RF power sources are well suited to deposit semiconductors and insulators. All the guns are equipped with pneumatically controlled shutters that needs to be opened before deposition. These guns hold 2” diameter targets. The tool

is also capable of performing back sputtering on the substrates by RF reverse bias, which is useful to clean the substrate or remove oxide layers. Along with these capabilities, reactive sputtering is also possible to grow dielectric thin films like SiN_x. Reactive sputtering is performed by injecting gases like N or O during deposition of semiconductors or metals. Like many other vacuum systems, the main sputtering chamber is connected to a load lock through a gate valve, which helps in quicker sample loading without compromising the vacuum. The main chamber and the lock are each continuously pumped by turbo molecular pumps that are connected to mechanical pumps. The robust vacuum systems ensure that the base pressure in the sputtering chamber is always $< 6.66 \times 10^{-6}$ Pa. When further chamber conditioning treatments are performed, the vacuum can reach the low 10^{-7} Pa range. The chamber conditioning involves deposition of gettering materials like Ti and Al followed by a bake-out step using heating straps. The substrates are mounted on a substrate holder made up of Inconel. The substrates can be heated up to 800°C and therefore heating during deposition or annealing after deposition of the films can be performed in vacuum to prevent oxidation.

Figure 10: (left) Orion 5 Sputter Deposition Tool used to synthesize metallic films. (right) Magnetron sputtering guns having copper targets. Pictures courtesy of AJA International.

3.1.2 Photolithography

The first step of photolithography is to spin coat the wafer with a layer of photoresist. Photoresist spinners/spin coaters are rotated at very high speeds (around 4000 rpm) to spin coat the wafer with photoresists by centrifugal force. The thickness of spin-coated layer depends mainly on two parameters, viz. photoresist viscosity and rotation speed. AZ 4620 and AZ 3312 photoresists were used for photolithography involved for synthesis of multimodal microstructure and MEMS device fabrication. AZ 4620 coats a layer of 6–8 μm thick resist depending on the rotation speed of chuck. This resist is used for device fabrication when 200 μm thick Si wafer needs to be etched in Deep Reactive Ion Etching (DRIE) tool. AZ 3312 is quite commonly used to coat 1 μm thick layer for intricate patterns that need better resolution. The patterning of multimodal architectures was performed using AZ 3312 photoresist as they provide better resolution during photolithography. Before spin coating the photoresist, HMDS (HexaMethlyDi-Silazane) was spin coated on the wafers to provide better adherence of photoresist with the wafer. After the photoresist was spin coated, a soft bake at 100°C was performed allow the evaporation of solvents.

UV exposure is the second step in a photolithography process. After the wafers are spin coated with photoresist and soft baked, a mask aligner tool (EVG 620) is used to align the chrome mask with the wafer. The chrome masks are designed in AUTOCAD and procured from an external vendor. The open regions in the mask are the regions where photoresist is exposed to UV radiation. After the wafer is aligned to the alignment marks on the mask, the UV lamp is turned on to expose the wafer to UV light. Exposures of 50 mJ/cm^2 and 500 mJ/cm^2 are provided for 1 μm and 8 μm thick photoresist. Thereafter, the exposed photoresist is developed using AZ 300MIF to obtain the patterned photoresist layer.

3.1.3 Dry/Wet Etching

After the photoresist is exposed and developed, the pattern needs to be transferred to the underneath layer. Depending on the underneath layer present, dry or wet etching is performed. Dry

etching is an etching method where a plasma of reactive/non-reactive gases is used in vacuum chamber along with power applied to the plates. No liquid chemical is involved in this process. On the other hand, wet etching is the method where etching is performed using the liquid chemical etchants. Wet etching is performed in the cases where the layer underneath cannot be etched using dry etch method. For example, Fe or Cu cannot be etched using dry etching, therefore, they need to be etched using a wet etch process.

The tool (PlasmaTherm PT 790) uses plasma of CHF_3 and O_2 gases to etch SiNx using a combination of physical and chemical etching as shown in Fig. 11. It was used to etch the SiNx layer underneath the photoresist. The wafer is kept on a graphite electrode inside the vacuum chamber to accelerate the plasma ions towards the wafer. The power and pressure used for this process was 50 W and 6.6 Pa. The advantage of dry etching is that it etches anisotropically, i.e., the etch rate of the material in the direction of the incident plasma is much higher than the etch rate in the orthogonal directions. Apart from reactive ion etching, this tool is capable of sputter etching. In case of thin films (< 50 nm) that cannot be chemically etched, Ar plasma can be used to physically remove (sputter) the thin film. Silver was sputter etched using this tool.

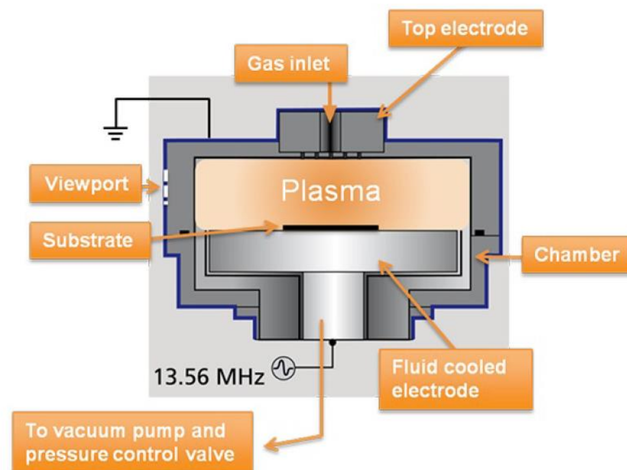

Figure 11: Schematic of the RIE chamber. The reactive gases are used to etch metal films. Picture courtesy of Oxford Instruments.

After the pattern is transferred from photoresist to the metal/SiNx layer, the fabrication of MEMS device is performed by etching silicon with high aspect ratio features. The MEMS devices are fabricated by deep etching while ensuring that the walls of the device structures remained vertical. STS Advanced Silicon Etcher was the tool used for this purpose. It uses a Fluorine-based chemistry and the “Bosch” process to achieve extremely anisotropic etch features (Fig. 12) [46].

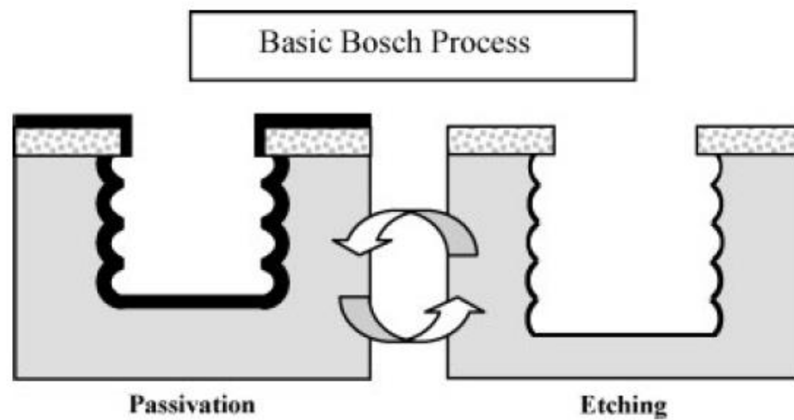

Figure 12: Schematic representation of the two step Bosch process [46].

The Bosch process is two-step process where the first step involves the deposition of a thin passivation layer of C_4F_8 (Teflon). The purpose of Teflon layer is to protect the side walls of the MEMS device. After the passivation of side walls, a SF_6 based plasma is created inside the vacuum chamber to etch the exposed silicon regions of the wafer. The other regions on the wafer are covered with the photoresist that acts as an etch mask. In the etching step, the SF_6 ions are accelerated towards the wafer by applying RF power. Physical sputtering and chemical etching occur simultaneously. The plasma ions are accelerated in a direction normal to the wafer surface and sputters off the passivation layer of Teflon and chemically etches away Si atoms. However, the passivation layer on the side walls is not sputtered away and therefore, protects the vertical walls from undercutting. F-based chemistries are very well known to etch Si where the reaction yields SiF_4 as a gaseous reaction product, which can be pumped out. Multiple etch/passivation

cycles are repeatedly performed until the Si wafer is etched through and freestanding metals films are obtained. The etch rate obtained during this process is around 2-2.5 μm/min. The etch/passivation times used are 6 s/8 s.

As mentioned earlier, wet etching methods were used where dry etching could not be performed. The wet etchants used for Cu and Fe are differently diluted nitric acid (HNO_3). Cu was etched using 1:3 HNO_3:Water and whereas Fe was etched using 1:100 HNO_3:Water. The etch rate for both Cu and Fe are 70 – 80 nm/min. The solution is continuously stirred during etching.

3.2 MEMS Tensile Testing Device

The MEMS device obtained from the fabrication was used to conduct uniaxial tensile tests on the co-fabricated freestanding thin films. The steps involved in the fabrication of a device and an optical image of the device is shown in chapter 6.

3.3 Microstructural Characterization

Microstructural characterization of the films was performed using XRD, TEM and EBSD. TEM characterization was performed using a JEOL 2010F transmission electron microscope, whereas EBSD scans were performed in a Zeiss Auriga dual beam focused ion beam/scanning electron microscope.

X-ray Diffraction is a non-destructive technique that uses X-rays for structural characterization of materials. It can provide information on crystalline phases, orientation, thickness of thin films and multilayers, structural properties like residual strain, grain size and phase composition. A Cu-Kα X-ray source is used to focus an X-ray beam on the sample through filters and divergence slits. The beam interacts with the sample and gets diffracted. The diffracted beam is then detected by a detector. The texture and quality of epitaxial growth was characterized by high resolution XRD (Panalytical X'pert Pro) using Cu-Kα radiation with parallel beam optics (10

mm mask, 0.25° divergence slits). θ-2θ, ω and Φ scans were performed to identify the growth orientation of the film and its epitaxial relationship with the SC Si wafer.

TEM is a microscopy technique in which an electron beam is transmitted through a specimen to form an image. Due to the limited transparency of the electron beam, samples thinner than 100 nm are most used. Heterostructured metallic films were characterized using a JEOL 2010F to obtain bright field images and selected area diffraction patterns.

SEM is a microscopy technique in which an image is captured by rastering a focused electron beam. Secondary electrons (SE) have limited mean free path in solids due to their very low energies (~50 eV). Therefore, secondary electrons escape from the top few nanometers of the sample surface. Secondary electron-based imaging was used to characterize the surface topography of the heterostructured metallic films. EBSD is a SEM-based microstructural characterization technique used to obtain information about the crystal orientation, structure, phase in a material. Since the sample is tilted at 70° from horizontal towards the diffraction camera, some electrons entering the sample backscatters. The escaping electrons exit near to the Bragg conditions and diffract to form Kikuchi bands corresponding to lattice diffracting crystal planes. Each band is then indexed individually by the Miller indices of the diffracting plane that forms it. Zeiss SEM/EBSD was used to perform orientation mapping. The parameters used for the scans were 20 KV electron voltage, 120 μm aperture and 20 mm working distance. TSL OIM Data Collection and Analysis software was used to obtain the EBSD maps.

CHAPTER 4

SYNTHESIS OF HETEROSTRUCTURED METALLIC FILMS WITH PRECISELY DEFINED ARCHITECTURES DIRECTLY ON Si SUBSTRATES

4.1 Introduction

Strength-ductility trade-off is a well-known phenomenon in metals [47], wherein an increase in strength usually comes at the expense of ductility. For example, homogeneous NC metals exhibit considerably higher strengths compared to their CG counterparts [4] but typically have uniform elongations of less than 5% due to the lack of effective strain hardening mechanisms [22,28]. Heterostructured metals such as those with bimodal or multimodal microstructures, in contrast, exhibit strain hardening rates that are comparable to CG metals and offer the promise of unprecedented strength-ductility synergy [10,14,20,44]. Nevertheless, methods to reproducibly synthesize heterostructured metals with robust microstructural control are still elusive. Here, a broadly applicable method is described to synthesize heterostructured metallic films with precisely defined architectures by exploiting two distinct forms of film growth (epitaxial and Volmer-Weber) simultaneously. This approach enables rapid validation of microstructural designs to enhance the properties of heterostructured metals and provides a platform to create functional thin films and 2D materials with tailored phase morphologies and microstructures.

Heterostructured metals, which are composed of domains that vary in size from a few nanometers to several micrometers, encompass a wide range of microstructural designs including multimodal microstructures [48], gradient microstructures [49–51], harmonic structures [18] and hierarchical microstructures [52,53]. These materials were synthesized through a variety of processing routes including thermomechanical treatment of cold worked metals [9], severe plastic deformation and sintering of powders [38,54], surface mechanical attrition/grinding treatment [13,42] and electrodeposition [55]. A common feature that links the different manifestations of heterostructured metals is the presence of plastically hard and soft domains, which leads to steep, internal plastic strain gradients even under macroscopically uniform deformation. The plastic strain

gradients are accommodated by the generation of highly dense networks of geometrically necessary dislocations (dislocations of same sign) which enhance the strain hardening rate and delay necking and fracture during tensile deformation.

But despite the considerable progress achieved in synthesizing heterostructured metals and understanding their deformation mechanisms, several challenges remain with regard to optimizing their mechanical and physical properties [32]. The primary challenge, perhaps, is controlling not only the size and volume fractions of the soft and hard domains but also their spatial distribution and connectivity, simultaneously and independently. This is essential to understand how the interplay between these parameters affect the strength-ductility synergy of heterostructured metals. An associated, but equally important issue, is the ability to produce these materials in a reliable and repeatable manner [32].

In this chapter, a novel method has been described which overcomes the challenges related to microstructural control and reproducibility, and enables the facile synthesis of metallic films with multimodal architectures, wherein the average size, volume fraction, spatial distribution and connectivity of fine and coarse grains can be explicitly defined.

4.2 Experimental Method

Synthesis Method

SC Si wafers (200 μm thick, 4-inch diameter) were cleaned in piranha solution (3 parts of Sulfuric acid and 1 part of 30% Hydrogen Peroxide) to remove organic residues and the wafers were dipped in 49% Hydrofluoric acid (HF) for 30 seconds to etch the native silicon dioxide layer. The wafers were then transferred to a LPCVD SiN_x deposition chamber within 15 minutes to deposit a 10-20 nm thick SiN_x layer with uniform coverage (±5 Å). The SiN_x coated wafers were patterned using photolithography and reactive ion etching (RIE). A 1 μm thick photoresist (AZ 3312) layer was spin coated at 3000 rpm, soft baked at 105°C for 1 minute and exposed to UV light (intensity

of 60 mJ/cm^2) through a patterned mask. The photoresist was then developed in AZ 300 MIF developer to create multimodal patterns on the photoresist. The photoresist was used as a mask to etch the SiN_x layer in RIE (50 sccm CHF_3, 5 sccm O_2, 7.33 Pa pressure, 50 W power) and transfer the patterns. Thereafter, the wafer was immersed in a heated photoresist stripper (AZ 400T) at 100 ^oC for 15 minutes to cleanly remove the photoresist. After photoresist removal the wafer was again immersed in 49% HF solution for 30 seconds to etch the silicon dioxide formed due to atmospheric exposure. The HF etch also passivates the surface with hydrogen atoms for 30-60 mins in atmosphere and prevents oxidation. The wafer was then transferred to a sputtering chamber within 5-10 minutes for metal deposition. Metal depositions (Cu and Fe) were performed at base pressures below 1.33 x 10^{-5} Pa, 100 W power and 0.4 Pa Ar pressure using an AJA Orion 5 sputtering system.

Microstructural Characterization

Microstructural characterization of the multimodal films was performed using XRD, TEM and EBSD. The texture and quality of film growth was characterized by high resolution XRD (Panalytical X'pert Pro). θ-2θ, ω and Φ scans were performed to identify the growth orientation of the SC and its epitaxial relationship with the SC Si wafer. TEM characterization was performed using a JEOL 2010F transmission electron microscope, whereas EBSD scans were performed in a Zeiss Auriga dual beam focused ion beam/scanning electron microscope. TSL OIM Data Collection and Analysis software was used to obtain the EBSD maps.

4.3 Results and Discussions

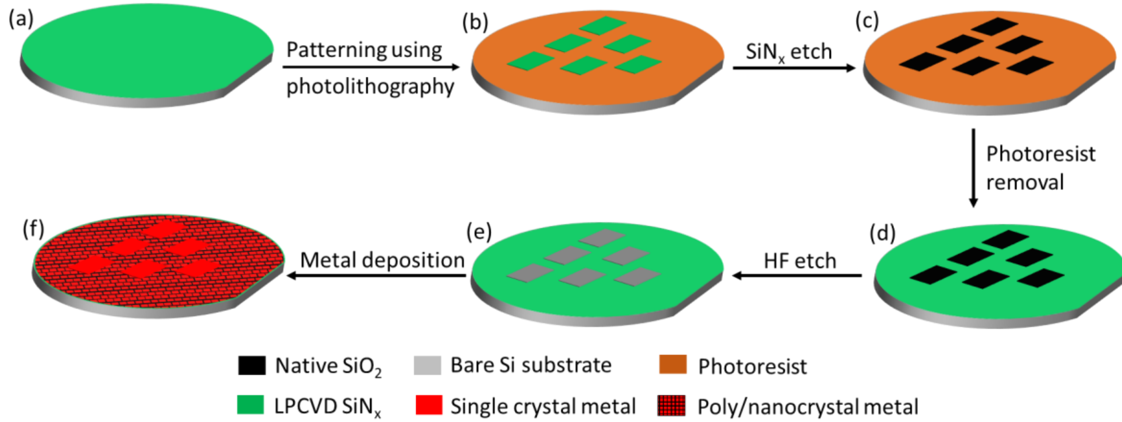

Figure 13: Synthesis of metallic films with multimodal microstructures. (a) A thin, amorphous SiN_x layer (10-20 nm) is deposited on a SC Si wafer using low pressure chemical vapor deposition (LPCVD). (b) Photolithography is used to define the desired multimodal microstructural design. (c) SiN_x layer is etched using reactive ion etching (RIE) to expose the underlying Si substrate at specific regions. (d) Photoresist is removed using a photoresist stripper. (e) The wafer is immersed in 49% HF solution to etch the silicon dioxide on the wafer surface. Exposure to HF passivates the Si surface with hydrogen for 30-60 mins and prevents it from reoxidizing. (f) The patterned wafer is transferred to a sputtering chamber within 5-10 minutes to deposit the metallic film with multimodal microstructure.

Fig. 13 shows the schematic of the synthesis method to obtain metallic films with multimodal microstructures. The basic idea is to create well defined monocrystalline and amorphous (SiN_x) regions on a SC Si wafer to grow the metallic films with the desired microstructural pattern. During metal deposition on the patterned Si wafer, the film grows via Volmer-Weber mechanism in the regions where SiN_x is present, resulting is a polycrystalline microstructure [56]. In contrast, the film grows epitaxially on the H-terminated Si regions if there is good lattice matching, which leads to the formation of SCs. Thus, the resulting metallic film is

composed of monocrystalline and polycrystalline regions as defined by the photolithography pattern. In this work, Cu and Fe were chose for demonstration since they grow epitaxially on Si(100) and Si(111) substrates even at room temperature [57,58].

An important criterion to generate heterostructured metals by this method is the presence of two types of substrates simultaneously. Out of the two types, one substrate needs to favor the epitaxial growth and the other needs to favor polycrystalline growth. Cu and Fe were chosen as the ideal candidates for the deposition as they grow epitaxially on Si SC substrates and in polycrystalline fashion on a polycrystalline/amorphous substrate. Both Cu and Fe were deposited on the patterned substrates containing SiN_x and Si regions. The microstructural characterization of each metal is shown below.

Cu grows epitaxially on hydrogen-terminated Si (100) substrate by evaporation [59], sputtering [57] and electrodeposition [60]. It grows through nucleation of epitaxial islands followed by their growth and coalescence [61]. Interestingly, Cu can also be grown epitaxially on Si (100) with intact native oxide layer using HiPIMS process [62]. On an amorphous substrate like SiNx, Cu grows as a polycrystalline film minimizing the surface energy and interfacial energy. The epitaxy of Cu film and its quality were examined through XRD followed by the characterization of heterostructured Cu film by TEM and EBSD as shown below.

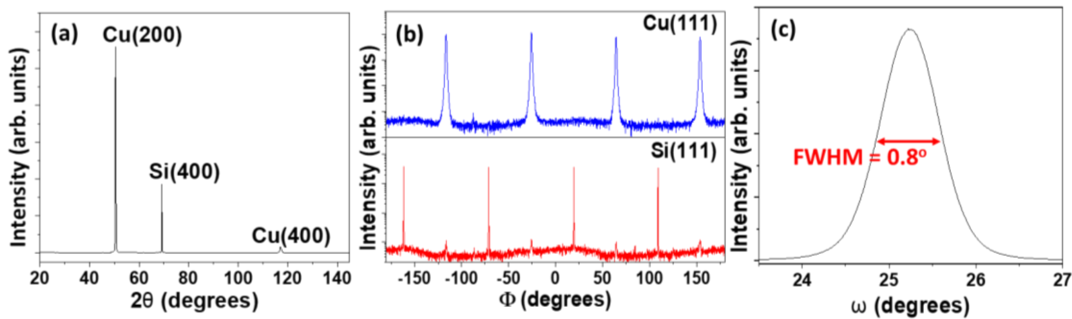

Figure 14: (a) θ-2θ XRD scan of epitaxially grown 1 μm thick Cu film on Si(100) substrate. (b) ϕ scan showing Cu(111) and Si(111) reflections while rotating the wafer about [100] axis. Note that the Intensity is in logarithmic scale. (c) Rocking curve (ω scan) of Cu(200) peak.

Fig. 14a-c shows the XRD characterization of a Cu film that was grown epitaxially on a Si(100) wafer. The θ-2θ scan (Fig. 14a) shows high intensity peaks at 50.51°, 69.10° and 117.03° which correspond to Cu(200), Si(400) and Cu(400) planes, respectively. No other peaks are present, which indicates a strong (100) out-of-plane texture for the Cu film. To ensure that the Cu film was grew epitaxially and not just a highly textured polycrystal, a ϕ scan was performed. Fig. 14b shows Si(111) and Cu(111) reflections obtained by rotating the Si wafer about the [001] axis. Four peaks, each 90° apart, are observed for Cu and Si due to the four-fold symmetry about [001] that results in the reflection of the four (111) planes. However, Si peaks are separated by 45° from Cu peaks which indicates that the Cu(100) plane is rotated by 45° with respect to the Si(100) plane. Therefore, the epitaxial relationship is $(100)_{Cu} \parallel (100)_{Si}$ and $[100]_{Cu} \parallel [110]_{Si}$. The 45° rotation occurs to reduce the lattice mismatch from 33% to 6%, [57] as explained in Fig. 17. In addition, a ω scan was performed to determine the quality of epitaxial growth. The rocking curve of Cu(200) peak obtained from ω scan (Fig. 14c) revealed a relatively small FWHM of 0.8°, which confirms that the epitaxial growth was of high quality. For reference, the FWHM value of the Si(400) peak from the nearly perfect SC Si wafer was 0.2°.

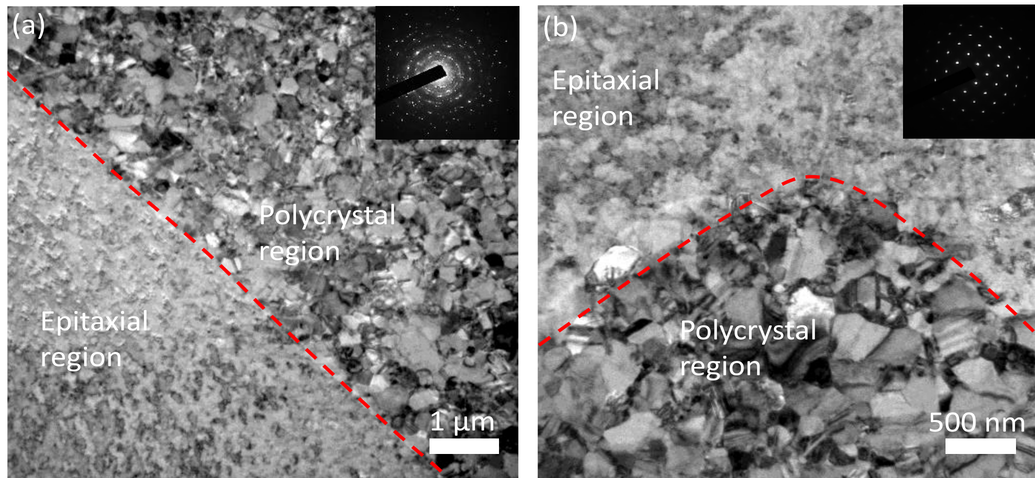

Figure 15: (a, b) Bright field TEM image of Cu film with bimodal microstructure at lower and higher magnifications. SADP of the polycrystalline and epitaxial region is shown as inset in (a) and (b).

After confirming that Cu grew epitaxially on Si(001), the microstructure of a 250 nm thick Cu film with bimodal microstructure (Fig. 15a-b) was directly imaged using TEM. The TEM analysis showed that the polycrystalline region was composed of grains ranging from 80 – 380 nm in size (mean diameter, d_m = 220 nm). Several twins were observed in these grains and the selected area diffraction pattern (SADP) showed a random in-plane texture. In contrast, a SADP taken along [100] zone axis revealed a SC -like diffraction pattern in the region where Cu grew epitaxially.

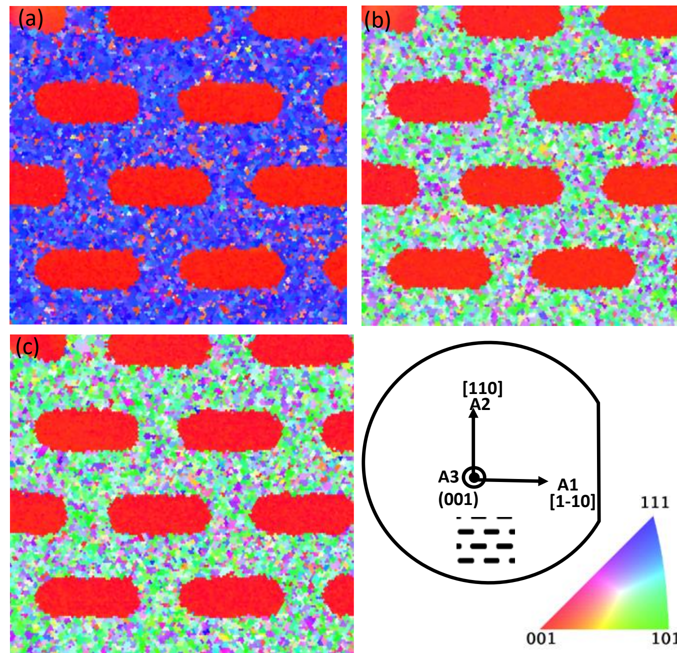

Figure 16: EBSD maps of a 250 nm thick bimodal Cu film along out-of-plane direction (a) and along two mutually perpendicular in-plane directions (b, c). The color-coded orientation for the EBSD maps in (a-c) is shown in the standard triangle (right, lower panel) along with a schematic that shows a Si (100) wafer represented with the directions and pattern shown on it.

The epitaxially grown Cu was monocrystalline was also confirmed using EBSD. Fig. 16 show the orientation of a Cu film with bimodal microstructure along three mutually perpendicular directions. The epitaxially grown Cu islands have a single orientation along all three directions

([100], [010], [001]). The polycrystalline region shows a (111) out-of-plane orientation, which is the preferred growth texture for Cu, whereas the in-plane orientations are random.

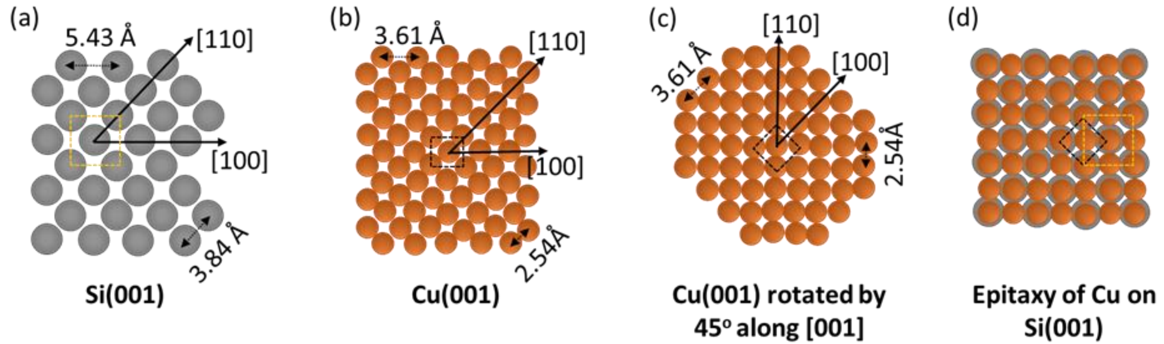

Figure 17: Schematics of the plan view of (a) top layer of Si (100) (b) top layer of Cu (100) (c) Cu (001) layer rotated by 45° along [001] (d) Cu atoms with respect to the Si atoms after epitaxy is formed. Si atoms are represented in grey and Cu in orange.

Figs. 17a-d shows a schematic of the arrangement of Cu and Si atoms. Fig. 17a and 17b corresponds to a plan view of Si (001) plane and Cu (001) respectively. Si has a diamond cubic structure and Cu has FCC structure. The interatomic distance between Si atoms along [110] is 3.84 Å, while along [100] is 5.43 Å. For Cu, the interatomic distance atoms along [110] is 2.54 Å and along [100] is 3.60 Å. If [100] and [110] of Cu and Si are matched, the lattice mismatch exceeds 33% which is not suitable for epitaxial growth. To reduce the lattice mismatch and thus the interfacial strain energy, it is highly favorable for Cu (001) to rotate by 45° for epitaxial growth. This is shown experimentally through XRD and EBSD techniques. Fig. 17c shows Cu (001) plane rotated by 45° along [001] such that $[110]_{Si} \parallel [100]_{Cu}$ and $[100]_{Si} \parallel [110]_{Cu}$. Fig. 17d shows that the Cu atoms are stretched to maintain epitaxy introducing tension in Cu layer.

To demonstrate the generality of this method, Fe films with multimodal architectures were also synthesized on Si(111) wafers since Fe grows epitaxially on H-passivated Si(111) substrates [58,63]. In addition, Fe films should show a smaller grain size in the polycrystalline regions since it

has a higher melting temperature and, consequently, lower atomic mobility at RT. As a result, there would be a greater contrast in grain size between the polycrystalline regions and the SC domains. Fig. 18a shows a high resolution θ-2θ scan of an epitaxially grown Fe film with distinct peaks at 28.45°, 94.93°, 137.24° that correspond to Si(111), Si(333) and Fe(222) planes, respectively. As in the case of Cu, a ϕ scan was performed to ensure that Fe film was a SC and not a highly textured polycrystal. The ϕ scan (Fig. 18b) for Si(220) and Fe(220) reflections, obtained by rotating the Si wafer about the [111] axis, showed three high intensity peaks corresponding to the three (110) planes at 35.26° to [111].

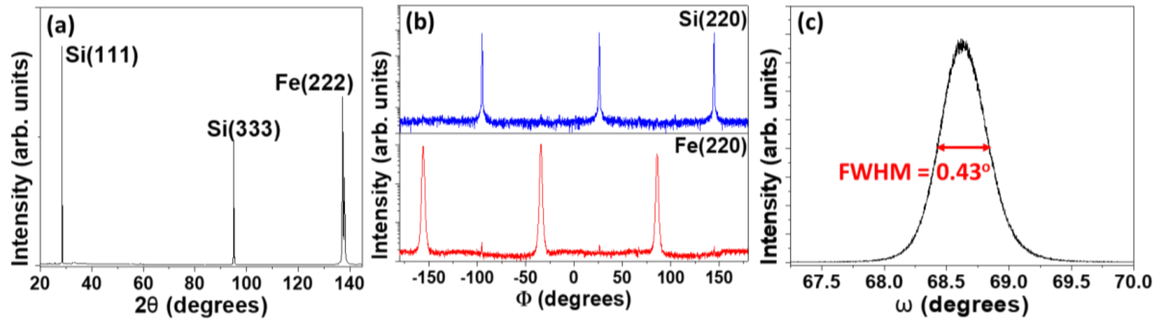

Figure 18: (a) θ-2θ XRD scan of a 1.56 μm thick epitaxially grown Fe film on Si(111) substrate. (b) ϕ scan showing Si(220) and Fe(220) reflections as the sample is rotated about [111] axis. Note that the Intensity is in logarithmic scale. (c) Rocking curve of Fe(222) peak.

In addition, the Fe film also showed three peaks of much lower intensity 60° apart from high intensity Fe peaks and in alignment with the Si(220) peaks, which indicates the presence of another Fe(111) variant. These high and low intensity peaks correspond to the twinned and aligned epitaxy of Fe on Si(111) substrates[63], as explained in Fig. 21. The aligned epitaxy corresponds to $[110]_{Si} \parallel [110]_{Fe}$ whereas twinned epitaxy corresponds to $[110]_{Si} \parallel [1\bar{1}0]_{Fe}$. Nevertheless, the substantially larger intensity of the peaks corresponding to the twinned variant indicates that it is the dominant variant. Moreover, the relative intensity of the aligned variant sharply decreased with increasing film thickness as shown in Fig. 19, which indicates that its growth is suppressed beyond

a few tens of nanometers. More importantly, the (111) rocking curve for the Fe film (Fig. 18c) showed a FWHM of just 0.43°, which attests to the high quality of the Fe SC. In fact, given the instrumental broadening (~0.2°) the actual FHWM value is considerably smaller.

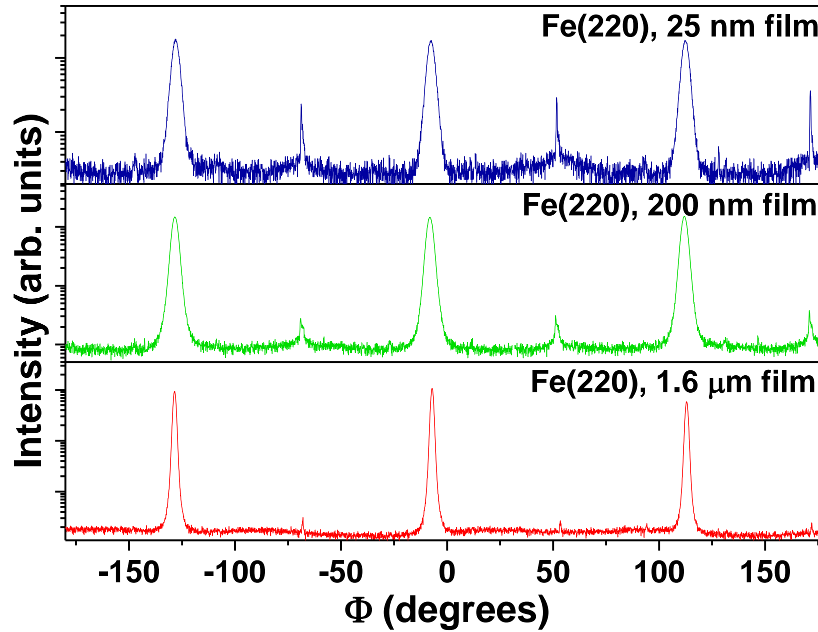

Figure 19: ϕ scans of 25 nm, 200 nm and 1.56 μm thick Fe films showing Fe(220) reflections while rotating the sample about the [111] axis. The higher intensity peaks correspond to twinned epitaxy of Fe(111) on Si(111). Note that the Intensity is in logarithmic scale.

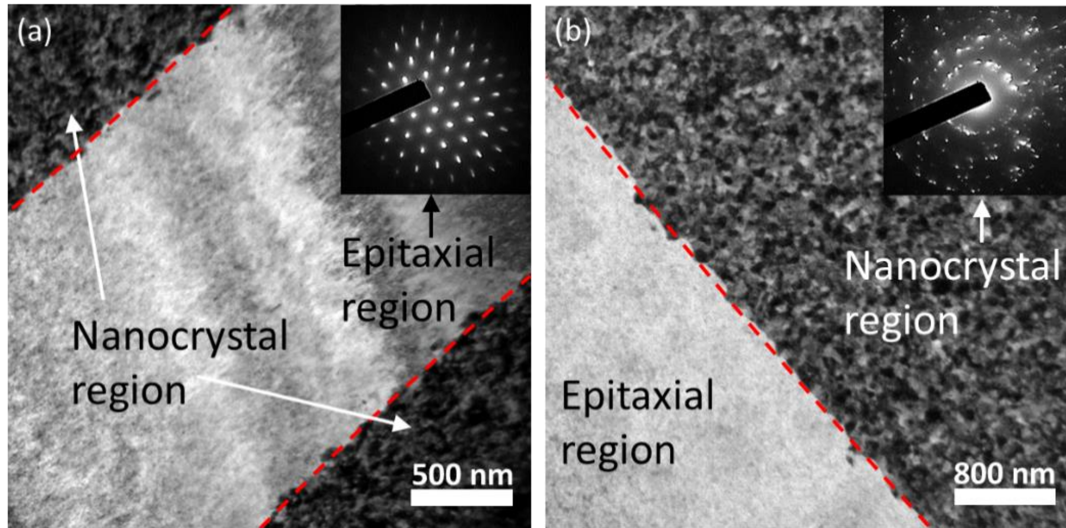

Figure 20: (a, b) Bright field TEM micrographs of a 175 nm thick Fe film with bimodal microstructure at lower and higher magnifications. SADP of the monocrystalline and polycrystalline region is shown as inset in (a) and (b).

The TEM micrographs (Figs. 20a-b) of a 175 nm thick , freestanding Fe film with bimodal microstructure revealed extremely fine grains ranging from 10 nm – 60 nm ($d_m \sim$ 23 nm) in the polycrystalline region. The SADP from the polycrystalline region showed a random in-plane orientation of the grains and no preferred texture. On the other hand, SADP taken from the epitaxial region along the [111] zone axis showed a SC-like diffraction pattern. Bend contours were observed in the epitaxial region due to the buckling of the freestanding film.

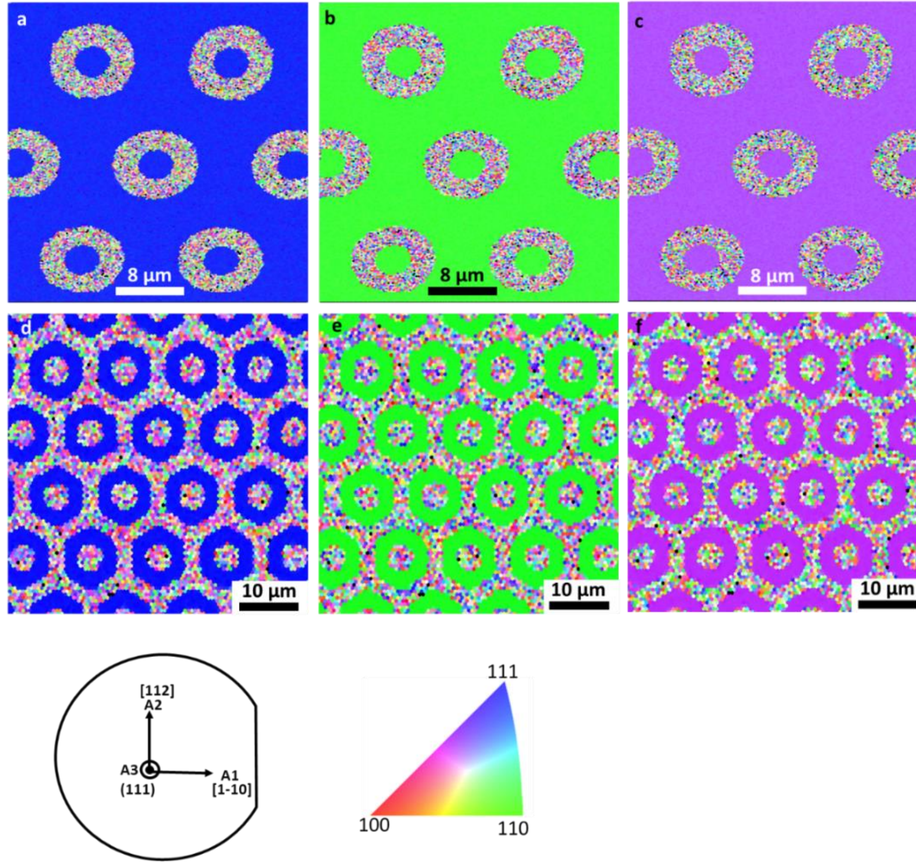

Figure 21: (a-f) EBSD maps of a 175 nm thick Fe film along out-of-plane direction (a) and along two mutually perpendicular in-plane directions (b, c). The film is composed of three distinct regions – the SC matrix, the NC rings and monocrystalline circular regions enclosed by the rings. (d-f) EBSD maps of a 175 nm thick Fe film with a NC matrix punctuated by monocrystalline ring structures. The color-coded orientation for the EBSD maps in (a-f) is shown in the standard triangle along with a schematic that shows a Si (111) wafer represented with the directions and pattern shown on it.

Fig. 21 shows EBSD maps of two different Fe films with contrasting architectures. The first film (Figs. 21a-c) has a monocrystalline matrix embedded with NC ring patterns. This architecture is defined by three distinct length scales (L) - the monocrystalline matrix (L > 10 µm), NC ring patterns ($L = d_m \sim 23\ nm$) and monocrystalline circular regions ($L = diameter = 3.6$ µm) enclosed by the NC

ring patterns. Note that the grain size in the NC region of the Fe films is below the resolution limit of EBSD, and hence the orientation information obtained in this region is not fully reliable. The second Fe film (Figs. 21d-f) is composed of a NC matrix embedded with hexagonally shaped rings, essentially mirroring the architecture of the first film. This capability to precisely define not just the volume fraction of coarse and fine domains but also the overall architecture is a unique aspect of this method, which is essential to experimentally validate microstructural designs to optimize the mechanical and physical properties of heterostructured metals.

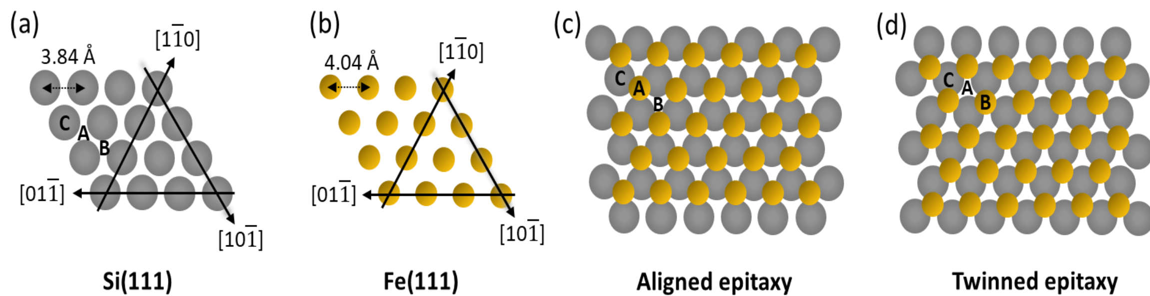

Figure 22: Schematics of (a) Si(111) plane. The possible locations of Si atoms in (111) planes (A, B, C) are shown. (b) Fe(111) plane. (c) Aligned epitaxy of Fe(111) on Si(111), which preserves the ABCABC stacking order. (d) Twinned epitaxy of Fe(111) on Si(111), which leads to ABCBAC stacking.

Fig. 22 shows plan view of atomic models of Fe (111), Si (111) and Fe (111) II Si (111) epitaxy. Si is a double atom motif with (0, 0, 0) and (1/4, 1/4, 1/4) arranged in an FCC lattice. The basic building block in Si is a tetrahedron where each Si atom is bonded to four neighboring Si atoms. When cleaved along (111) plane, each atom on this plane has a single dangling bond which binds with hydrogen on exposure to HF. The interatomic distance in Fe and Si along [110] is 4.04Å and 3.84 Å respectively. Therefore, to minimize misfit strain energy, atoms in Fe (111) are compressed along [110] to maintain epitaxy. Similarly, the interatomic distance in Fe and Si along [112] is 6.99

Å and 6.65 Å, respectively. Thus, a misfit strain of ~5% along [110] and [112] is observed in epitaxial Fe films.

4.4 Conclusions

In this chapter, a novel method is described that showed a pathway for the rational design of heterostructured materials. This method utilized two different modes of film growth. First, the growth of epitaxial film on an epitaxial substrate and second, the growth of polycrystalline film on polycrystalline/amorphous substrate. Using this method, heterostructured Cu and Fe films were synthesized directly on Si substrates by magnetron sputtering. The microstructural characterization was performed using XRD, TEM and EBSD. It was clearly demonstrated that the microstructural architectures could be precisely controlled by this method.

CHAPTER 5

SYNTHESIS OF HETEROSTRUCTURED METALLIC FILMS USING A BUFFER LAYER ON Si SUBSTRATES

5.1 Introduction

The method discussed in chapter 4 can be utilized for creating heterostructured films of metals (e.g., Cu, Fe, Ag) which grow epitaxially on single crystal Si substrates. However, the method cannot be used for metals which do not grow epitaxially (e.g., Ni, Cr, Ti) on Si substrates. In this chapter, it is shown that by introducing a buffer layer it is possible to grow heterostructured films of metals such as Ni and Cr.

The epitaxial growth of a film on a substrate depends on the crystal symmetry and the lattice mismatch between the film and substrate. Typically, a mismatch strain of 10% or lower is needed for a film to grow epitaxially. When the lattice mismatch is high, buffer layers can be used to reduce the interfacial strain energy and promote epitaxial growth. For example, epitaxial layers of GaN cannot be grown directly on sapphire substrate using MOCVD method due to a high lattice mismatch of 15%. By introducing a AlN buffer layer, which leads to a reduction of lattice mismatch strain to 2.5%, it is possible to grow epitaxial GaN layers [64]. Thin rutile (TiO_2) films are another commonly used buffer layer to grow epitaxial multifunctional oxides like (111)-oriented $SrTiO_3$, $SrCaTiO_3$ on GaN substrate by RF-plasma-assisted oxide molecular beam epitaxy [65]. A range of buffer layers, like Al_2O_3, Si_3N_4, AlN, SiC, GaN have used to overcome this difficulty [66–68]. ZnO film has a lattice mismatch of 18% with sapphire substrate due to which the quality of crystallinity is quite poor, and the film has high dislocation density. Various buffer layers like GaN, MgO, ZnS, and SiC have been successfully used to grow epitaxial ZnO layers [69–72]. Apart from oxide films, buffer layers also been utilized in the growth of epitaxial metallic films. Since silver shows low reactivity with other metals and grows epitaxially on Si (100), Si (110) and Si (111), it is quite commonly used to grow metallic films epitaxially which do not do so otherwise. Depending on the

substrate orientation and lattice mismatch, elements like Fe, V, Cu, Ti, Ni, Co can grow epitaxially on Ag buffer layer [73].

5.2 Experimental Method

The substrate preparation method for heterostructured Cr and Ni films is similar to the substrate preparation method for heterostructured Cu and Fe films. The wafer is patterned and then exposed to HF to avoid regrowth of native oxide layer. After exposure to HF solution, the wafer is immediately transferred to the sputtering chamber. First, a 20 nm buffer layer of Fe or Ag is deposited followed by Cr or Ni deposition on top. The sputter rate of each metal was calibrated using crystal thickness monitor prior to deposition. All metals (Fe, Cr, Ag, Ni) were deposited at 100 W and 0.4 Pa Ar pressure while rotating the substrate. The base pressure of the chamber before deposition was 6.66×10^{-6} Pa.

The microstructural characterization of the films was performed using XRD and EBSD. Cr epitaxial film was characterized by high resolution XRD (Panalytical X'pert Pro). θ-2θ, ω and Φ scans were performed to identify the growth orientation of the SC and its epitaxial relationship with the SC Si wafer. Heterostructured films were characterized using EBSD in a Zeiss Auriga dual beam focused ion beam/scanning electron microscope. TSL OIM Data Collection and Analysis software was used to obtain the EBSD maps.

5.3 Results and Discussions

In this section, the synthesis and microstructural characterization of heterostructured Cr and Ni films are discussed.

Cr on Fe/Si (111) substrate

The epitaxial growth of Cr was evaluated by three different kinds of XRD scans: θ-2θ scan, ω-scan and Φ-scan, as shown in Fig. 23. θ-2θ scan helps to identify the out of plane orientation of

the Cr film. In the case of an epitaxial film, only a single (111) Cr peak was observed along with Si peaks. This suggests the presence of a (111) texture. To investigate the in-plane orientation of Cr, Φ-scan of the film and the substrate was performed. The scan was done such that the (110) planes reflected while the sample was rotated about (111) axis. The three major and minor peaks correspond to (110) planes. Majority of the film showed an aligned epitaxy with Si whereas a small fraction showed twinned epitaxy. From XRD scans, Cr is observed to grow epitaxially on Fe with a cube-on-cube orientation relationship – Cr (111) ll Fe (111) and Cr [110] ll Fe [110].

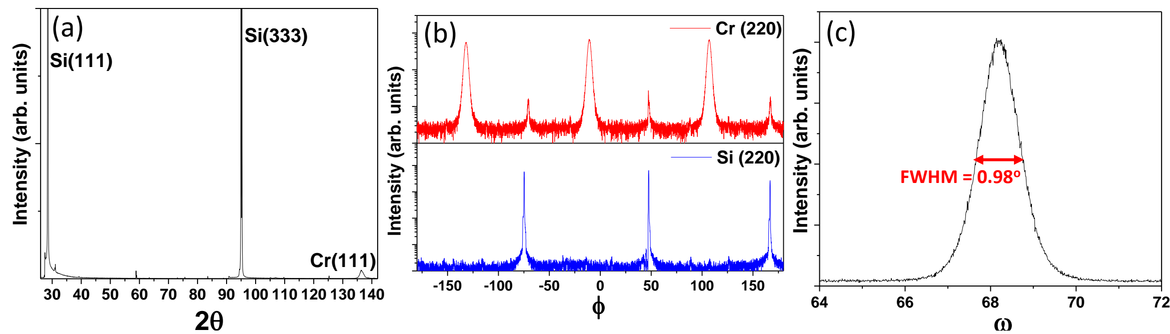

Figure 23: (a) θ-2θ scan of 200 nm epitaxial Cr grown on 20 nm Fe/Si substrate (b) ϕ scan of Si (220) (above) and Fe (220) (below) reflections while rotating the sample about [111] axis (c) ω-scan of Cr (111) peak

The heterostructured Cr film was characterized using EBSD which looked very similar to Fe as they grow with cube-on-cube orientation relationship. Fig. 24 shows a EBSD scan of a heterostructured Cr film with a nested structure. SC Cr forms a continuous global matrix which are embedded with isolated NC Cr ring patterns. These NC ring patterns serve as a local matrix for µm-sized circular SC Cr regions. As evident from the EBSD scans, the orientation of the SC Cr is the same in both the global matrix as well as the smaller circular regions, whereas NC domains showed no preferred orientation.

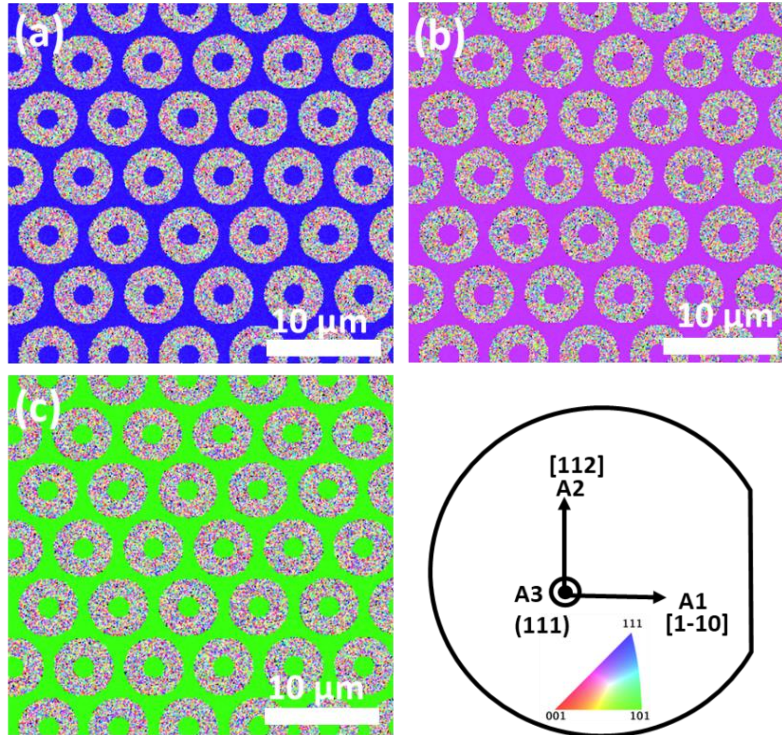

Figure 24: EBSD micrographs of a heterostructured Cr film deposited on a patterned Si/Fe substrate (a) along A3, (b) along A2 and (c) along A1. Schematic shows a Si (111) wafer represented with the directions shown on it. Color representation for each orientation is shown in the standard triangle.

Ni on Ag/Si (001) substrate

Typically, when buffer layers are used to grow epitaxial films, film deposition must be performed without breaking vacuum. Otherwise, an oxide layer is likely to grow on the buffer layer, which would disrupt epitaxial growth. However, if Ag is used as a buffer layer it can potentially be exposed to the atmosphere since it does not readily form a native oxide layer. To test whether this approach will work, the heterostructured Ni films with Ag buffer layers using a modified method was investigated, as shown in Fig. 25. In this modified method, Ag is directly deposited on Si and patterned for the deposition of the heterostructured Ni film, i.e., no SiN_x layer is used. This approach is advantageous because Ag has poor adhesion to SiN_x and the residual stress in the Ni film

promotes delamination of the Ag buffer layer from the Si substrate, which would be detrimental to fabricating freestanding heterostructured Ni films for tensile testing using MEMS devices.

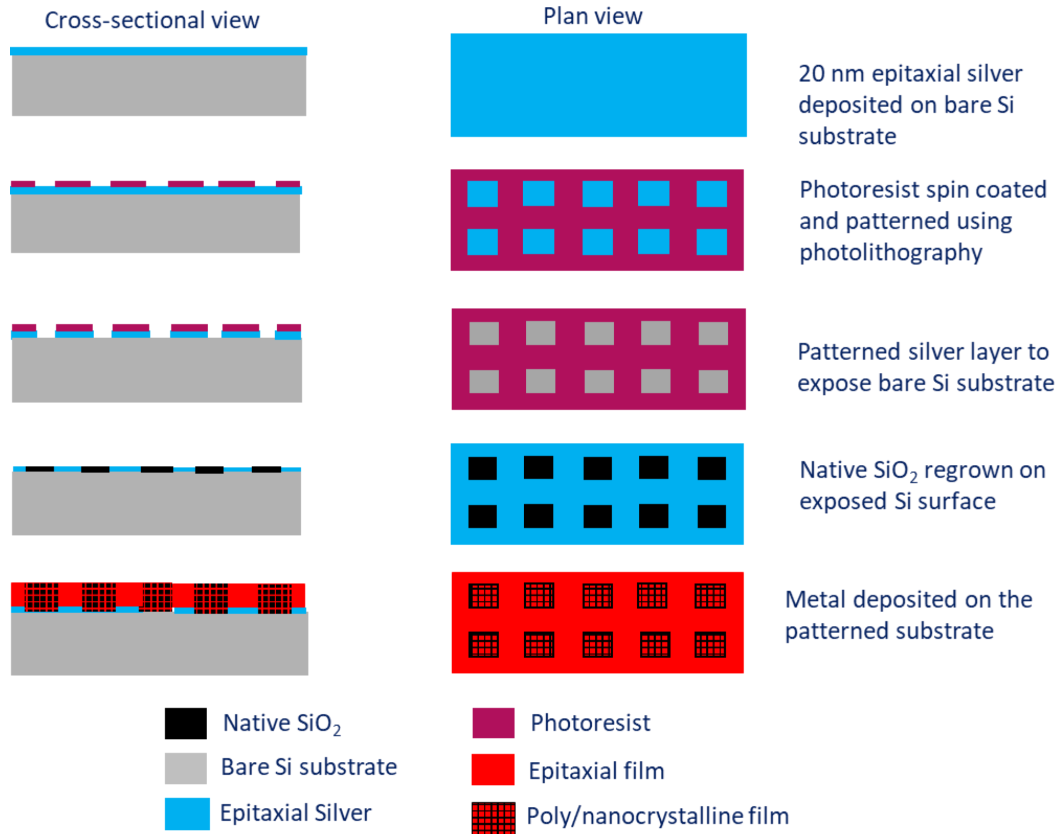

Figure 25: Schematic representation of each step involved in the synthesis of heterostructured Ni film through microfabrication processes.

In this modified method, 20 nm Ag layer was first deposited at 150°C on a Si (001) wafer that was exposed to HF for 30s to etch native oxide and avoid its regrowth. Then, 1 µm photoresist was spin coated and soft baked for 1 minute at 105°C on the Si/Ag wafer. The photoresist was exposed to UV radiation through a photomask, containing various patterns, at 35 mJ/cm^2. This was then followed by development of the exposed photoresist in AZ 300 MIF solution for 1 minute, followed by hard baking at 120°C for 3 minutes. The hard bake helps evaporate excess solvent in the photoresist, which prevents the photoresist from hardening during the dry etch process. The

exposed silver was then sputter etched in the PT 790 tool at 50W for 10 minutes using Ar ions. Once silver is etched, photoresist was stripped off by ultrasonicating it in acetone for 5 minutes. The wafer was dipped in isopropanol alcohol (IPA) immediately after ultrasonication to avoid acetone residue on the wafer. Finally, the wafer was dried using nitrogen and then transferred to the sputtering chamber. Before Ni deposition, the surface of Ag was sputtered off to remove any oxide layer or residue. The wafer was then heated up to 150°C at which Ni deposition was performed.

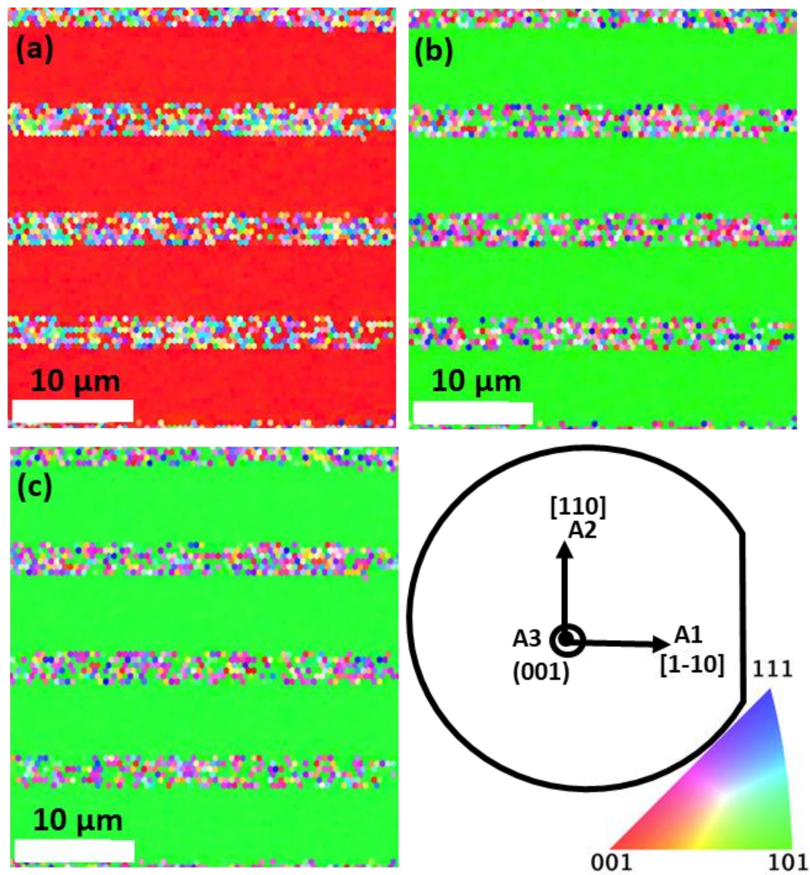

Figure 26: EBSD micrographs of a heterostructured Ni film deposited on a patterned Ag/Si substrate (a) along A3, (b) along A2 and (c) along A1. The microstructure contains a parallel arrangement of NC and epitaxial regions. Schematic shows a Si (001) wafer represented with the directions shown on it. Color representation for each orientation is shown in the standard triangle.

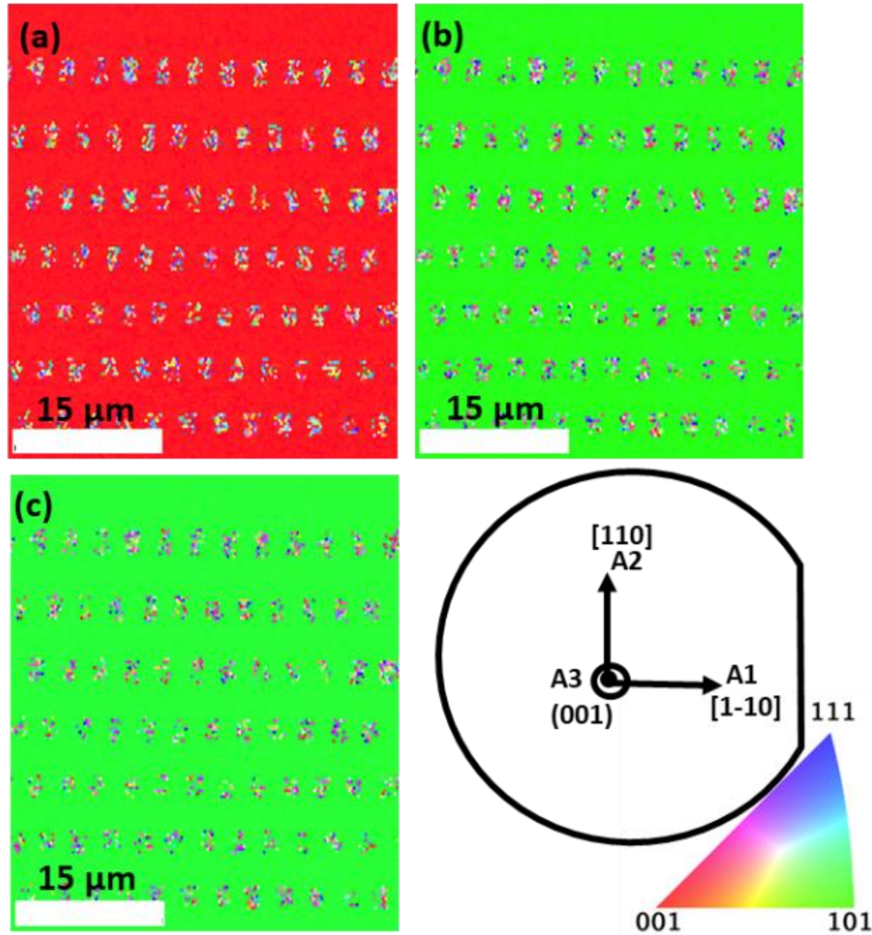

Figure 27: EBSD micrographs of a heterostructured Ni film deposited on a patterned Ag/Si substrate (a) along A3, (b) along A2 and (c) along A1. The microstructure contains NC domains within an epitaxial matrix. Schematic shows a Si (001) wafer represented with the directions shown on it. Color representation for each orientation is shown in the standard triangle.

After the film deposition, the microstructural characterization was performed using EBSD as shown in Fig. 26 and Fig. 27. Two different architectures are shown here: one with a parallel architecture and the other with a SC matrix and isolated NC domains. Ni grew epitaxially on Ag with a (001) out-of-plane orientation while it grew in a polycrystalline fashion on SiO_2. The observed epitaxial relationship between Ag and Ni is $(100)_{Ni} \parallel (100)_{Ag}$ and $[110]_{Ni} \parallel [110]_{Ag}$.

5.4 Conclusions

In this chapter, a different approach to synthesize heterostructured metallic films with precisely defined architectures was described. Here, a buffer layer was used for the growth of SC films that cannot be grown epitaxially on Si directly. This was demonstrated for two such systems – Cr and Ni – using Fe and Ag buffer layers. In addition, for Ag buffer layer, an alternate fabrication method was described, which circumvents the problems associated with the poor adhesion between Ag and SiN_x/SiO_2. This alternate approach is useful to fabricate freestanding heterostructured metals films for tensile testing using MEMS devices.

CHAPTER 6

FABRICATION OF MEMS TENSILE STAGE FOR TESTING FREESTANDING HETEROSTRUCTURED METALLIC FILMS

6.1 Introduction

In the previous two chapters, different methods to synthesize various heterostructured metallic films (Cu, Cr, Fe and Ni) were described. In this chapter, the fabrication of MEMS tensile testing stages for the mechanical testing of heterostructured Fe films is described. This method can be easily adapted to other metallic films as well. The fabrication of MEMS tensile testing stage with freestanding heterostructured Fe films involved basic microfabrication methods like photolithography, metal etch, Si deep etching, photoresist removal. The section 6.2 discusses the challenges encountered during the fabrication process and how they were resolved. The section 6.3 discusses the step-by-step description of the processes involved in the fabrication is described using schematics.

6.2 Challenges Addressed During MEMS Stage Fabrication

The first observation after Fe deposition was the presence of high residual stresses. When 1.56 μm thick films were deposited on 200 μm thick Si substrate, the wafers visually showed large curvature. These intrinsic residual stresses are generally observed in as-deposited films at room temperature [74–76]. They are divided in two different categories: type I (low mobility materials like Cr, Ni) and type II (relatively high mobility materials like Ag, Cu, Au, Al). In type I materials, high tensile stresses are induced due to the island coalescence. During coalescence, nearby islands deform elastically to reduce the surface energy of the islands by the formation of a grain boundary between the islands. The tensile stresses is inversely dependent on the grain size and could reach several GPa when the grain size is smaller than 10 nm [77]. In type II materials, the tensile stresses are low when islands coalesce compared to type I materials. Due to higher atomic mobility of these

materials, surface diffusion and grain boundary diffusion tend to densify the grain boundaries lowering the tensile stresses in these films.

When type I materials are sputter deposited, the tensile stress increases with the increasing thickness. Similar effect was observed in 1.56 μm thick Fe film deposited by the visual appearance of concave curvature of the substrate after deposition. The presence of high tensile stresses in Fe was not suitable for the fabrication of MEMS tensile testing stage. It posed problems during two microfabrication steps – photolithography and deep Si etching. Due to the curvature of wafer, it was difficult to properly align the wafer to the mask. A small misalignment of 4-5 μm caused misalignment of the patterned microstructure on the freestanding film which was not desirable as it affected the mechanical properties of the film. Another challenge with having high tensile residual stress was observed during deep Si etching. This step involves etching of Si from the bottom to the top leaving behind a freestanding Fe film which is exposed to the atmosphere from the backside. The high tensile stress in the freestanding film gets relieved by deforming the alignment and force-sensing beams. However, when the beams are too stiff, they do not allow the film to relieve stress by deforming the beams. In such cases, if the stress reaches fracture strength, the film tends to fracture. In addition, the tensile stresses promote oxidation, which can drastically alter the mechanical behavior of the films. Therefore, there was a need to eliminate residual stress in the films generated during deposition to successfully fabricate MEMS tensile testing stage.

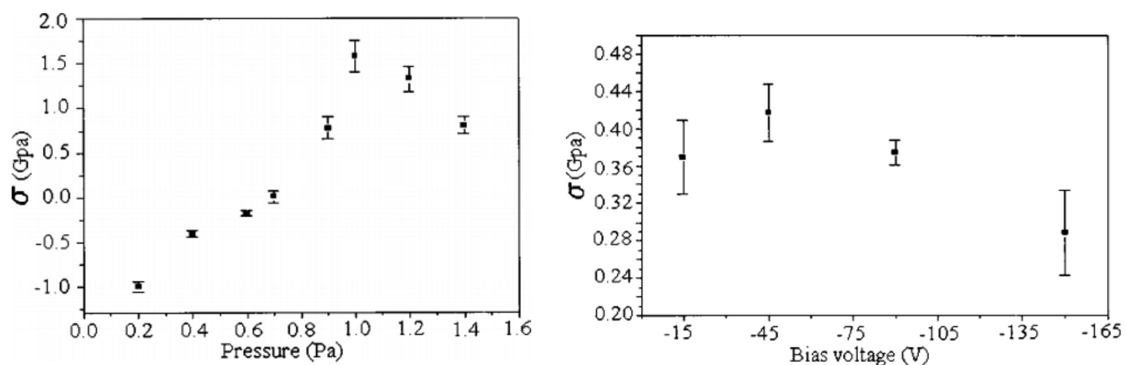

Figure 28: Variation of residual stress with (left) Ar pressure with substrate kept at zero potential (right) bias voltage between -15 V and -165 V with constant deposition pressure at 0.266 Pa [78].

The residual stress strongly depends on the substrate temperature, pressure of the sputtering gas and the application of reverse bias to the substrate during deposition as shown in Fig. 28 [79,80]. The depositions could not be performed at high temperatures since it would cause grain growth in the NC domains. Varying the sputtering gas pressure and applying bias seemed like the viable possibilities. Fig. 28 shows the change in residual stress with Ar pressure and reverse bias voltage applied to the substrate for Ni [78]. It can be observed from the graphs that lower Ar pressure and higher bias helps to reduce the tensile stress. After a few iterations, the deposition parameter for Fe films were optimized to ensure lower residual stress. The parameters used were 100 W power, 0.13 Pa Ar pressure and -120 V bias. Using these deposition parameters helped reduce the curvature of the substrate after Fe film deposition and eliminated the misalignment problem during photolithography. Furthermore, the Fe film did not fracture or oxidize after being released from the substrate. To ensure that the Fe film did not oxidize even during long-term atmospheric exposure, a 15 nm Al passivation layer was deposited on the top and bottom of the film.

Once the problem of residual stress was addressed, metal etch posed its own challenges. During fabrication, a clean etch was of utmost importance to pattern the Fe film. Fe cannot be dry etched using Cl chemistry since Iron chloride is not volatile at room temperature. Fe reacts with chlorine plasma and leaves a residue on the surface that prevents further etching. Therefore, it had to be etched using a wet etch method. Several chemicals like dilute HCl, dilute HNO_3 etc. can be used to etch Fe. Generally, the less diluted acids etch much faster but leads to undercutting of the samples and photoresist damage. On the contrary, highly diluted acids etch at much slower rates and could consume hours to etch a thick film. Therefore, to optimize the dilution and the etch rate, many samples of similar thicknesses were patterned and etched with various dilutions. Fe was observed to etch cleanly in a highly diluted nitric acid 1:100 (HNO_3:H_2O) with an etch rate of 50

nm/min. Undercutting was avoided by continuous stirring of the solution during etching. Clean and macroscopically smooth edges of the samples were obtained. The etch rate of SC and NC domains was different, as expected. Therefore, all the samples were patterned such that their edges consisted only of NC domains.

In addition to overcoming the challenges involving residual stresses and etching, the MEMS stage itself had to be redesigned to enable the testing of the thick Fe films. During a tensile test, the force on the sample is measured by multiplying the stiffness of the force-sensing beams by their displacement. If the stiffness of the beams is too high, their displacement will be quite low, which would worsen the force resolution. On the other hand, if the beam stiffness is small, the displacements will be large, which will lead to a non-linear force-displacement response. Moreover, a large displacement of the force-sensing beams will also necessitate a large displacement of the alignment beams, which will lead to excessive bending of the support structure. In such a case, the stiffness of the force-sensing beams will continuously vary with its displacement, which will make it significantly more complicated to estimate the force on the sample. To avoid these complications, the beam thicknesses were optimized to obtain good force resolution while avoiding non-linearities. The optimal stiffness of the force-sensing beams was estimated by taking into account the stiffness of the sample during elastic deformation and its yield stress. The elastic stiffness and yield strength of 1.56 μm thick Fe film (with 375 μm gauge length and 80 μm width) was around 60 KN/m and 1400 MPa, respectively. For these values, a maximum displacement of 12-14 μm for the force-sending beams avoided non-linearities and provided adequate force resolution. The stiffness corresponding to these parameters was calculated to be ~15 KN/m, which was obtained by changing the length and thickness of the force-sensing beams appropriately.

6.3 Fabrication of MEMS Tensile Testing Stage

Once the heterostructured metallic film was deposited on the wafer using the method, described in chapter 4, the wafer was taken through a series of processes for MEMS stage

fabrication. A step-by-step procedure to fabricate the MEMS tensile testing stage with the freestanding heterostructured Fe film is described below:

1) The first step was to perform photolithography on the wafer with the heterostructured Fe films using a photomask with MEMS device pattern. 1 μm thick photoresist (AZ 3312) was spin coated on the top and 8 μm thick photoresist (AZ 4620) was spin coated on the bottom, at 3500 rpm and 2000 rpm, respectively, using spinner as shown in Fig. 29. The photoresist was then soft baked at 105°C for 1 min (AZ 3312) and 8 min (AZ 4620), respectively.

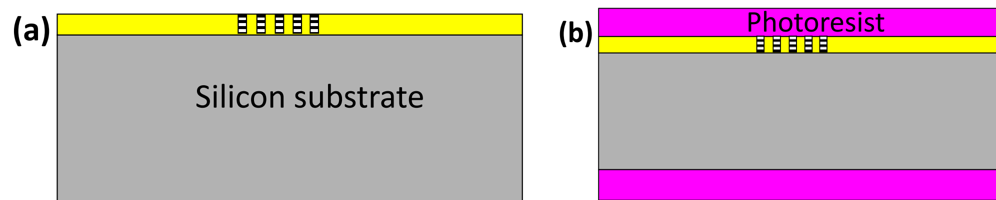

Figure 29: (a) A heterostructured Fe film deposited on a wafer by magnetron sputtering. (b) The wafer was spin coated with photoresist on the front and backside.

2) Later, the wafer was taken through UV radiation exposure (EVG 620) and photoresist development. For this, the markers on the front side of the wafer with 1 μm thick photoresist was aligned with the markers of the frontside mask. Once the alignment was performed carefully, the photoresist was exposed to a radiation of 50 mJ/cm^2 and only the alignment markers were developed in developer (AZ 300 MIF) for 1 minute. Next, the backside of the wafer with 8 μm thick photoresist was aligned to the frontside alignment markers. The photoresist was then exposed to a radiation at 500 mJ/cm^2. The major difference between a frontside mask and backside mask was the presence of a dog-bone shaped sample in the fronside mask. After exposure, first the 8 μm thick photoresist was developed for 8 minutes followed by the development of 1 μm thick photoresist for 1 minute as shown in Fig. 30a. The device patterns were then transferred from photoresist layer to metal layer

by etching Fe using a dilute nitric acid etchant as shown in Fig. 30b. While etching, the patterned photoresist masked other regions from being etched.

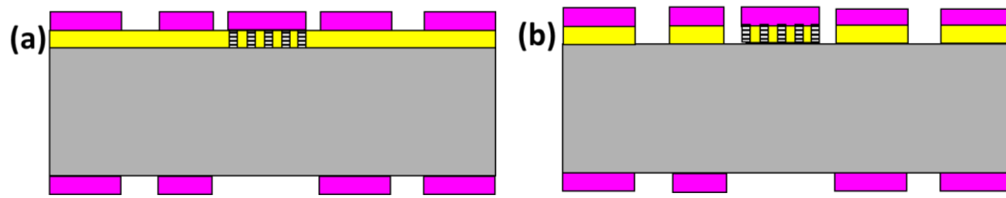

Figure 30: (a) Photoresist patterned on the front and backside by exposure to UV light followed by photoresist development. (b) The pattern is transferred to metal layer by etching Fe using dilute nitric acid.

3) Finally, 200 μm Si was etched from the bottom to the top using a deep Si etcher (STS ASE). This etch was anisotropic in nature that helped in maintaining the dimensions of each structure within the device. Once the heterostructured Fe films were free of Si and the devices were clean, they were detached from the wafer and placed in oxygen plasma (Asher) to remove the photoresist from the front and backside of the devices as shown in Fig. 31.

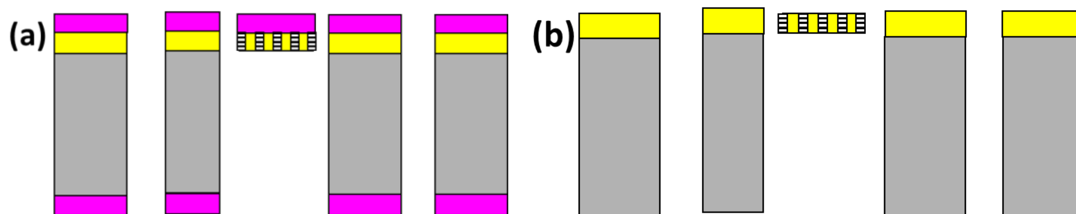

Figure 31: (a) Anisotropic etching of Si using Si deep etcher from the back all the way to the top. (b) Photoresist removal from the top and bottom.

The MEMS stage along with a freestanding sample obtained from the fabrication is shown in Fig. 32. It contains a pinhole at each end. One end is fixed, and the other is pulled by a piezo actuator at a specific displacement rate to achieve the desired strain rate on the sample. The U-

beams and alignment beams in the MEMS stage ensure the sample is uniaxially loaded. The gauges G1 and G2 are connected to the ends of the sample and therefore the change in the gap between them provides a direct measure of sample elongation (and strain) during the tensile test. The relative displacement of G2 with respect to G3 gives the deflection of the force sensing beams, from which the force (and stress) on the sample can be calculated. A high-resolution CMOS camera was used to capture images of the gauges during sample deformation, and the movement of gauges were tracked using an image correlation MATLAB code to obtain the stress-strain curves.

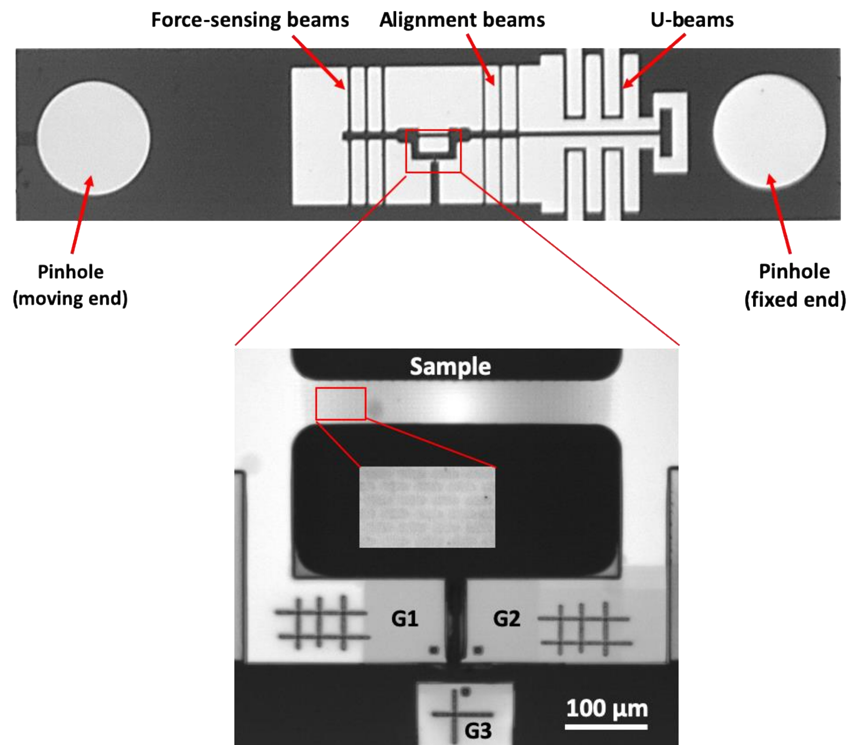

Figure 32: Optical image of a MEMS tensile testing stage with a co-fabricated, freestanding metal sample with a bimodal microstructure. The sample and gauges (G1, G2 and G3) are shown at higher magnification in the bottom figure. An enlarged view of a part of the sample is shown in the inset. The darker regions in the inset are SCs whereas the lighter regions are polycrystals.

6.4 Conclusions

This chapter discusses the fabrication of MEMS tensile testing stage with the freestanding heterostructured Fe film. First, the challenges related to the fabrication of MEMS stage with Fe films, which included residual stress development during deposition, etching of Fe film by wet etching and the design of photomask to test thicker films, were described. Residual stress was relieved by lowering the Ar deposition pressure and applying a substrate bias. A wet etchant with optimized dilution was prepared to produce samples with smooth and uniform edges. The dimensions of the force-sensing beams were optimized to obtain adequate force resolution while avoiding non-linearities. The step-by-step process involved in the fabrication of MEMS stage was described. Finally, different architectural designs are illustrated that were mechanically tested (shown in the next chapter).

CHAPTER 7

MECHANICAL CHARACTERIZATION OF HETEROSTRUCTURED Fe FILMS

7.1 Introduction

Metals and metallic alloys used in structural applications typically need to possess a combination of good strength and ductility/toughness. One of the well-known methods to increase strength is via grain size refinement, as exemplified by the Hall-Petch relationship [81,82]. This strategy of grain size refinement culminated in the production of metals and alloys with UFG and NC microstructures. Severe plastic deformation techniques such as high-pressure torsion, equal channel angular processing is widely used to generate bulk-scale UFG and NC samples, whereas physical vapor deposition and electrodeposition are more commonly used for synthesizing UFG and NC thin films and coatings. These UFG/NC metals exhibit an order of magnitude increase in strength compared to their CG counterparts and exhibit a multiplicity of deformation mechanisms including generation and propagation of full and partial dislocations slip, deformation twinning and grain boundary sliding [1,2,83]. However, this increase in strength comes at the expense of ductility, a phenomenon often referred to as the “strength-ductility trade-off”.

The lower ductility observed in NC metals primarily arises from a lack of strain hardening ability [84,85], which leads to strain localization and early failure. When these materials are deformed, dislocations typically nucleate at a grain boundary and, because the grain size is very small, they travel across the grain and get annihilated at the opposite grain boundary before they can interact with other dislocations. Therefore, there is no accumulation of dislocations or formation of permanent dislocation networks within the grains, which prevents the hardening required to sustain uniform plastic deformation [6,7]. Hence, there is a concerted effort to develop strategies to improve the ductility and toughness of NC metals while retaining their strength.

One strategy that was proven particularly successful is the development of heterostructured metals and metallic alloys [9,86]. These materials, often referred to as heterostructured materials,

are comprised of domains/grains that have length scales varying from a few nanometers to tens of micrometers. In these materials, the larger grains are plastically soft but enable accumulation and storage of dislocations that leads to macroscopic strain hardening. The smaller grains, in contrast, primarily increase the strength. While the overall strength of heterostructured materials is smaller than that of NC materials, their substantially higher ductility and toughness make them more suitable for structural applications compared to NC materials [11,50]. It should also be noted that due to synergistic effects, the strength of heterostructured metals is notably larger than what is predicted from a simple rule-of-mixtures analysis [87].

Over the last two decades, various processing methods were developed to produce heterostructured materials, which include thermomechanical processing, surface mechanical attrition/grinding treatment (SMAT/SMGT) and consolidation of powders with widely varying grain sizes. Wang et al performed cryo-rolling of Cu followed by annealing to enable abnormal grain growth through secondary recrystallization [88–90], which resulted in a microstructure with μm-sized grains embedded in a UFG matrix. Similarly, Wu et al performed asymmetric rolling followed by partial recrystallization leading to the formation of micro-grained lamellae within a UFG matrix [44].

Although the aforementioned methods are all capable of producing heterostructured metals with high strength and good ductility, they also suffer from some limitations. For example, while they provide some control over the mean size and volume fraction of fine and coarse grains, they provide little or no control over their spatial connectivity or the overall microstructural architecture. Furthermore, some of these methods such as thermomechanical processing are sensitive to even small changes in the processing conditions, which makes it challenging to produce heterostructured metals in a reliable and repeatable manner. As a result, it is difficult to systematically probe the relationship between various microstructural parameters and the mechanical properties, which is essential to designing heterostructured metals with an optimal combination of strength and ductility/toughness.

A highly reproducible method is described in chapter 4, that is capable to synthesize metallic films with multimodal microstructures wherein the size, volume fraction and spatial connectivity of fine and coarse grains as well as the overall architecture can be precisely defined [91]. Here, the bimodal Fe films with three distinct architectures (parallel, series and wave-like) using this method were synthesized and their deformation behavior under tension was investigated. Furthermore, the effects of different microstructural parameters within each architecture were examined. The results showed that both the overall architecture as well as the geometry of dislocation slip in the coarse grains influenced the mechanical behavior of metallic films with bimodal microstructures.

7.2 Experimental Method

Synthesis Method

The architectural designs were made using the method described in chapter 4 and the tensile testing stages with freestanding heterostructured films containing these architectural designs were fabricated using the method described in chapter 6.

Microstructural Characterization

Microstructural characterization of the films was performed using TEM, XRD, EBSD and SEM. A 2010F JEOL TEM was used to obtain bright field images and selected area diffraction patterns from a 175 nm thin heterostructured Fe film. θ-2θ scan, ω-scan (rocking curve) and φ-scan of epitaxial Fe film were performed using a four-circle goniometer enabled Panalytical X'Pert Pro using Cu-Kα radiation with 0.25^o fixed divergence slits and 5mm incident beam width mask. θ-2θ scan was performed in the range of $20^o \leq \theta \leq 145^o$ with a 0.05^o step size and 1°/min scan rate. Rocking curves were collected from Fe (111) peak within a range of 3° with a 0.001^o step size at 0.5^o/min scan rate. The high resolution EBSD orientation scans were obtained using Zeiss Auriga focused ion beam scanning electron microscope (FIB-SEM)equipped with a EBSD detector. The step size used to capture the scans was 0.5 μm. The EBSD scan data was analyzed using OIM

analysis software. The Zeiss FIB-SEM was used to observe the surface topography of the heterostructured film by secondary electron imaging.

Mechanical Characterization

Freestanding films were co-fabricated along with MEMS tensile testing stage as described in hapter 6. During fabrication, Fe was etched by dilute nitric acid (1 HNO_3: 100 H_2O) at an etch rate of 50 nm/min. No visible roughness or serration was observed on sample edges, possibly due to the slow etch rate. Once the film was released from the substrate, a 15 nm Al passivation layer was also deposited at the bottom to avoid sample oxidation. The MEMS stage was configured such that all the samples were loaded along [112] loading direction of the coarse grains (SC domains). For applying uniaxial tension on the freestanding films, one end of the stage was fixed, and the other end was pulled at a constant velocity (~100 nm/s) using a piezo actuator. This actuator velocity corresponds to an average strain rate of ~10^-4/s on the samples. All the samples were monotonically loaded until failure.

7.3 Results

The heterostructured Fe films with three distinct bimodal architectures – parallel architecture (PA), series architecture (SA) and wave-like architecture (WA) were created – as illustrated in Fig. 33. All these bimodal architectures are composed of SC domains that grow on top of the bare Si regions in the patterned wafer and NC domains that grow on top of the SiNx regions. In the PA and SA samples, the loading direction is parallel and perpendicular to the interface between SC and NC domains, respectively. In the WA samples, SC and NC domains are arranged in wave-like pattern and the interface makes an angle of 45o with respect to the loading direction. Within each of these architectures, the widths of the SC (W_{SC}) and NC domains (W_{NC}) were varied while keeping the volume fractions of both domains at 50%. For the PA samples, the volume fraction of the SC and NC domains were also varied, while keeping W_{SC} constant.

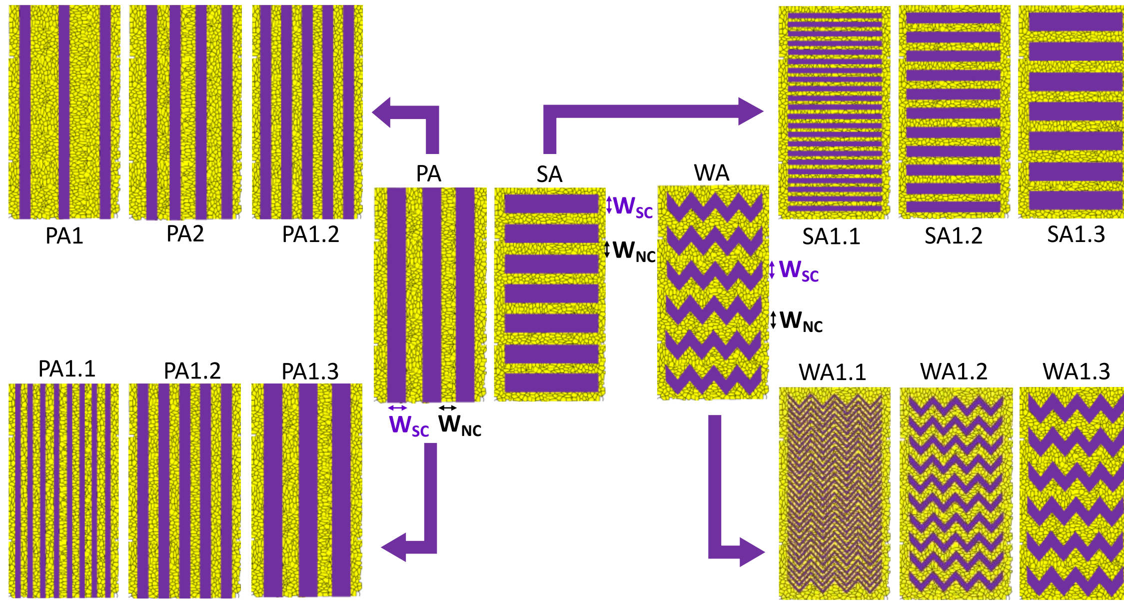

Figure 33: Schematic of Fe films with different bimodal architectures that were synthesized and tested. The purple color corresponds to SC domains while yellow color corresponds to NC domains. W_{SC} and W_{NC} are the widths of the SC and NC domains.

Table 1 provides the W_{SC} and W_{NC} values for every bimodal Fe sample tested in this study according to its designation in Fig. 33. In addition to these bimodal Fe samples, pure SC samples and pure NC samples were also synthesized to determine the mechanical properties of the SC and NC domains. All the samples tested had a gauge length of 375 μm, nominal width of 80 μm and a thickness of 1.56 μm. The edges of all the bimodal Fe samples were composed of NC domains to ensure that all the samples were etched in the same manner during patterning. These NC domains at the edges (~ 6 μm in width) are also included in calculating the volume fraction of the NC and SC domains in the bimodal Fe samples.

Table 1: List of bimodal Fe samples with their microstructural parameters and mechanical properties.

Sample	Architecture	W_{SC} (μm)	W_{NC} (μm)	NC volume fraction (%)	Yield strength (σ_y)	Strain to failure (ε_f)
PA1	Parallel	5	24.5	80	1160 MPa	2.64%
PA2		5	6.8	60	1005 MPa	2.46%
PA1.1		2.5	2	50	1030 MPa	2.13%
PA1.2		5	3.4		970 MPa	2.31%
PA1.3		10	8		895 MPa	2.15%
SA1.1	Series	2.5	2	50	1060 MPa	1.66%
SA1.2		5	3.4		1025 MPa	1.58%
SA1.3		10	8		1060 MPa	1.24%
SA1.4		15	11.5		1020 MPa	1.06%
WA1.1	Wave	2.5	2	50	900 MPa	1.04%
WA1.2		5	3.4		930 MPa	1.67%
WA1.3		10	8		960 MPa	1.44%

7.3.1 Microstructural Characterization

A detailed microstructural characterization was performed on the bimodal Fe films. In addition, EBSD was used to determine the orientation of the SC domains. Fig. 34 shows EBSD maps of bimodal Fe samples with the three different architectures that were investigated in this study. The maps are color-coded by the crystal orientation at each location with respect to three mutually perpendicular axis (2 in-plane and 1 out-of-plane). As evident from the EBSD maps, the SC domains have a [111] orientation along the z-axis (out-of-plane), while their [10] direction is aligned with the x-axis and [11] direction with the y-axis (loading direction). There was no indication of a second variant within the SC domain since EBSD is a near-surface technique which probes only the top 10-15 nm of the film (1.56 μm thick), and the second variant is present only at the bottom of the film for a few tens of nanometers. It is also important to point out that the EBSD data in the NC domains does not provide any reliable information since the grain size (~25 nm) is well below the resolution limit of EBSD.

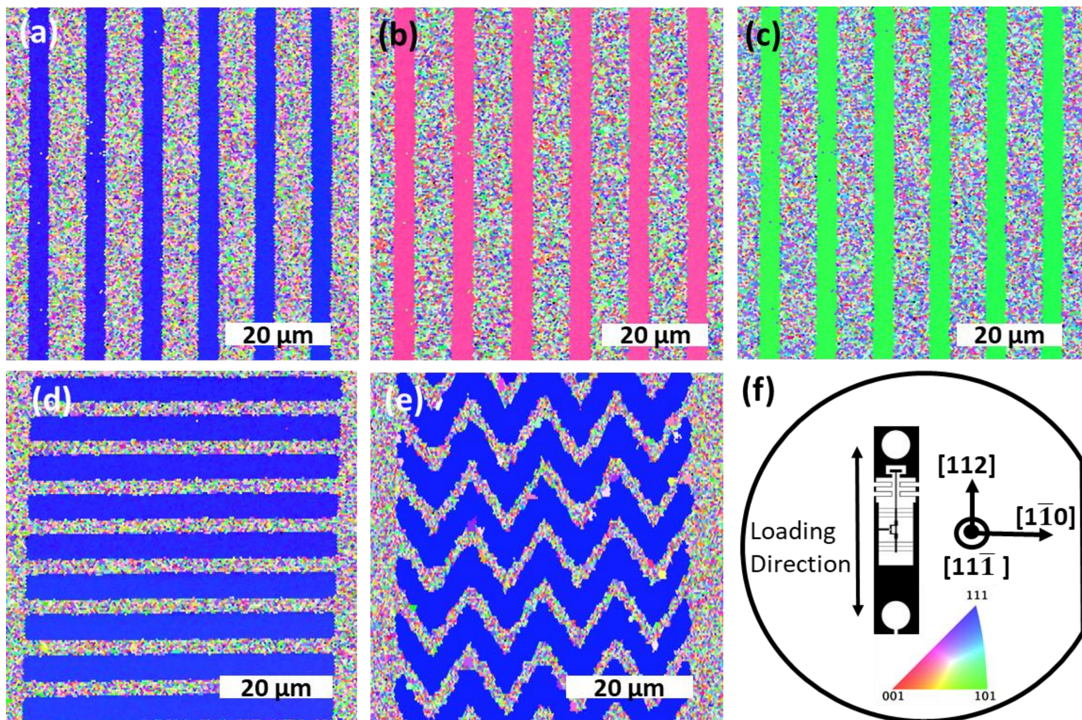

Figure 34: (a-c) EBSD maps of a bimodal PA film sample. The colors correspond to crystal orientation (see standard triangle in (f)) with respect to the out-of-plane direction (a) and two in-plane directions (b and c). (d, e) EBSD maps of a SA sample and WA sample showing their out of-plane orientation. (f) Schematic of a Si (111) wafer showing $[11\bar{1}]$, $[1\bar{1}0]$ and [112] directions. An image of the MEMS stage is superimposed to show its orientation with respect to the Si wafer.

In addition to EBSD, TEM was used to characterize the bimodal Fe films. Since electron transparency in the TEM is limited to a few hundred nanometers for Fe, a 175 nm thick film for this purpose was deposited. Fig. 35 shows a bright field TEM micrograph of the thinner bimodal Fe film containing SC and NC domains adjacent to each other. The grain size in the NC domain varied between 10 nm to 60 nm, with mean size of ~23 nm. Incidentally, the mean grain size for the 1.56 μm thick NC Fe film, estimated from the (110) XRD peak using the Scherrer equation, was ~25 nm. In other words, there was no significant change in the grain size for NC Fe as the film thickness was increased from 175 nm to 1.6 μm. The SADP obtained from the SC domain along the [111] zone axis showed a SC -like diffraction pattern, whereas the SADP from the NC domain showed a spotted ring-like pattern suggesting that grains are randomly oriented.

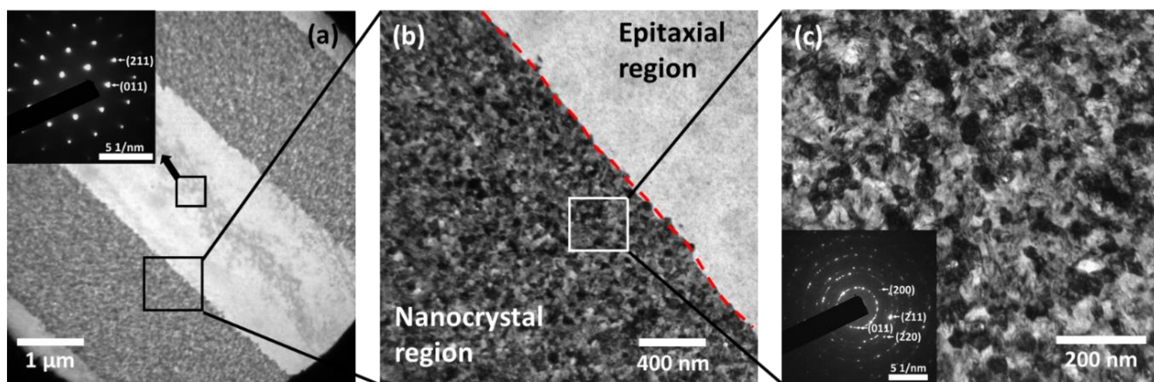

Figure 35: Bright field TEM micrograph of a 175 nm thick bimodal PA sample. SADP of the SC and NC domain are shown as insets in (a) and (c).

7.3.2 Mechanical Behavior of Bimodal Fe Films

The mechanical behavior of 12 different bimodal samples with three different architectures (5 PA samples, 4 SA samples and 3 WA samples) were examined as mentioned in Table 1. In addition, the stress-strain response of pure SC and NC samples was also measured. In the following subsections, the results were organized to highlight the effect of different microstructural parameters (volume fraction of SC and NC domains, size of the SC domains) as well as the overall architecture on the deformation behavior of the bimodal Fe films.

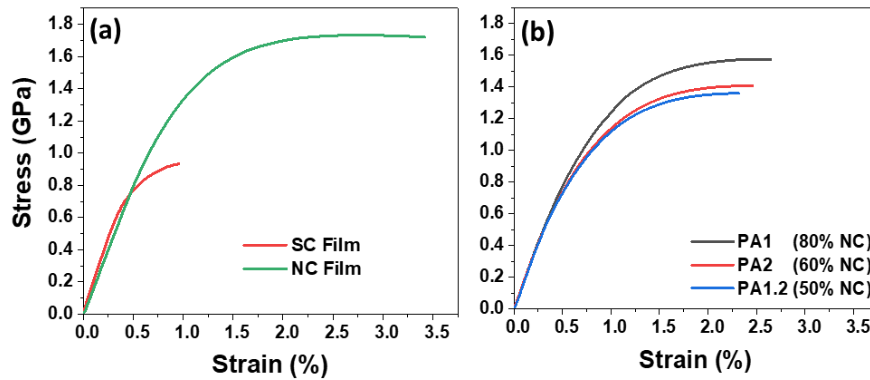

Figure 36: Stress-strain response of (a) pure SC and NC Fe film, and (b) bimodal PA samples with different volume fractions of NC domains.

The stress-strain response of the pure SC (loaded along [112] direction) and NC Fe film is shown in Fig. 36a. The Young's modulus of the SC and NC Fe film was 210 GPa and 170 GPa, respectively. The Young's modulus of the SC film is identical to the modulus of bulk Fe in the [112] direction, which attests to the accuracy of the stress-strain measurements. The lower modulus of the NC film is due to the large fraction of grain boundaries, which have higher compliance. The SC sample yielded around 850 MPa (stress at 0.2% offset strain) and almost immediately failed via strain localization. The NC sample on the other hand exhibited a higher yield stress (σ_y) of 1.35 GPa and a higher strain to failure ($\varepsilon_f = 3.4\%$). The NC sample also showed a gradual elastic-plastic transition and very little strain hardening, as is typical of NC metals.

Fig. 36b shows the stress-strain behavior of bimodal PA samples having different volume fractions of SC and NC domains. The NC volume fraction was varied from 50% - 80% by altering W_{NC} (see Table 1) while keeping W_{SC} constant at 5 μm. The data clearly indicates that increasing NC volume fraction leads to increasing strength. This is expected because the NC and SC domains have to co-deform in the PA samples, and the yield strength of the PA samples is determined by both domains. Similar to σ_y, ε_f was also highest for the PA sample with the highest NC volume fraction, which is unsurprising since the NC sample had a significantly higher ε_f than the SC sample. It is to be noted that since the grain size in the NC region is much smaller than W_{NC} and W_{SC} is constant, the difference in the stress-strain response between the three samples purely reflects the effect of NC and SC volume fraction.

Since the grain size (internal length scale) of the NC domains is much smaller than W_{NC} (external length scale) their behavior is solely dictated by the grain size. In contrast, W_{SC} (along with the sample thickness) is expected to significantly influence the behavior of the SC domains and, consequently, the bimodal samples. To elucidate the influence of W_{SC}, the samples with different W_{SC} within each architecture were tested, while keeping the volume fraction of the SC and NC domains at 50% each. Fig. 37 shows stress-strain data for PA, SA and WA samples with different W_{SC}. The data show contrasting trends that highlight how the interplay between the microstructural architecture and the length scale of the SC domains profoundly influence the stress-strain response. For instance, σ_y of the PA samples reduced by more than 130 MPa when W_{SC} was increased from 2.5 μm to 10 μm. Contrarily, σ_y increased by 60 MPa for the WA samples for the same change in W_{SC}. Interestingly, no clear trend in σ_y was seen in the SA samples even as W_{SC} was increased from 2.5 μm to 15 μm.

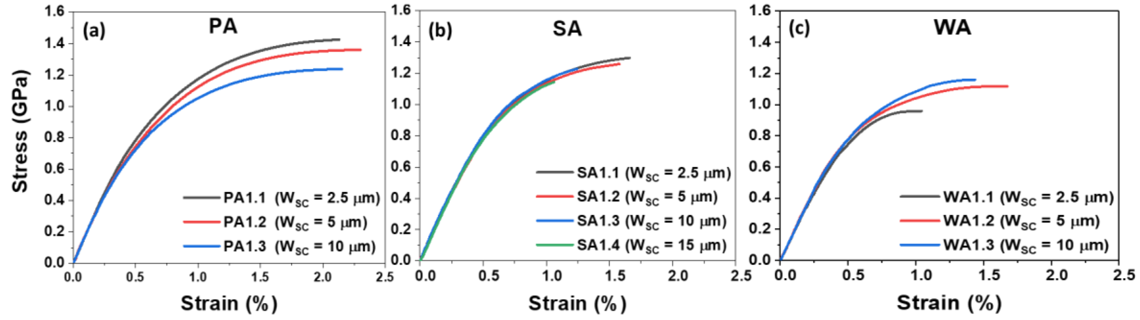

Figure 37: Stress – strain curves of (a) PA, (b) SA and (c) WA samples with different W_{SC} and equal (50%) volume fractions of NC and SC domains.

Changes in W_{SC} also induced notable differences in ε_f among the samples with different architectures. The PA samples exhibited no specific trend in ε_f with regard to W_{SC}, and these samples sustained at least 2% strain before failure. For SA samples, ε_f progressively decreased with increasing W_{SC}. Notably, ε_f was just over 1% for SA1.4 sample. In contrast to the SA samples, the WA sample with the lowest W_{SC} (2.5 μm) exhibited the smallest ε_f. In fact, this sample also had the lowest σ_y, which is highly counterintuitive since one would expect that the constraints arising from a small W_{SC} would strengthen the SC domains.

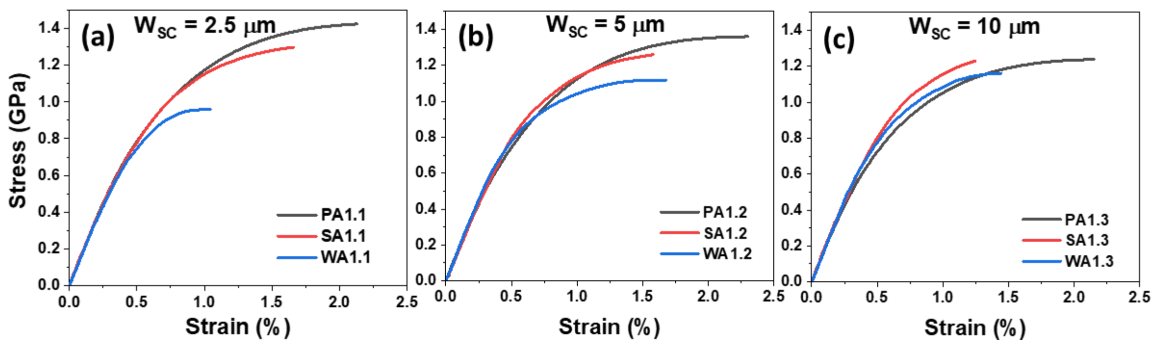

Figure 38: Stress – strain curves of bimodal samples with different architectures but equal volume fractions of SC and NC domains.

In Fig. 37, the changes in W_{SC} (length scale of the SC domains) altering the deformation behavior of samples within each architecture was described. However, it is also instructive to analyze how the deformation behavior varies across different architectures when W_{SC} and the volume fractions of the NC and SC domains are kept constant. Such an analysis would help clarify the role of microstructural architecture in determining the mechanical behavior of the bimodal Fe films. Towards this end, the stress-strain data from the bimodal samples with equal volume fractions of NC and SC domains across different architectures were analyzed (Fig. 38). Certain distinct trends emerge from this analysis. First, σ_y of SA samples is closer to that of PA samples for small W_{SC}. Second, as W_{SC} increases σ_y of WA samples becomes closer to that of the SA samples. Third, PA samples have the highest ε_f for all values of W_{SC}. Finally, the WA samples exhibited a greater tendency for strain localization (softening in the stress-strain response), irrespective of W_{SC}.

7.3.3 Deformation behavior and fracture of heterostructured films

To gain insights into the deformation mechanisms of the bimodal Fe films, the microstructure (Fig. 39) and fracture surface (Fig. 40) of samples from each architecture using SEM was imaged. The SEM observations clarified two key aspects of deformation in the SC domains. First, only two major slip traces were seen in all architectures. BCC metals can exhibit dislocation glide on multiple slip planes, viz., (110), (112) and (123). However, the presence of only two slip traces at 60° and 120° to the loading axis in the SC domains strongly indicates that dislocation activity was confined to {110} family of slip planes (Fig. 41). The specific slip systems are $(101)[\bar{1}11]$ and $(011)[1\bar{1}1]$ and both these systems have a Schmid factor of 0.41, which means that that they are equally likely to be activated. In this context, it is worth pointing out that previous studies have also revealed slip only on {110} planes in SC iron samples at RT under quasi-static loading conditions [92–94].

Second, the contrast from the slip traces was much starker in the case of WA samples compared to the PA and SA samples. The stronger contrast, which arises from surface height

difference between the slipped and unslipped regions, suggests that dislocation slip is more localized in the WA samples.

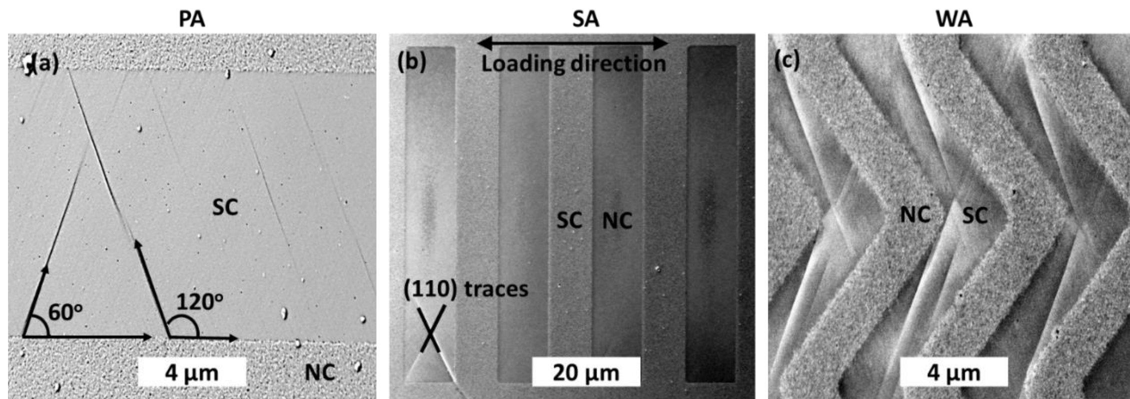

Figure 39: Deformed microstructure of a (a) PA, (b) SA and (c) WA sample. Slip bands with (110) traces are clearly visible within the SC domains.

The PA samples showed a spatially more uniform distribution of slip traces. An examination of the fracture surface of the PA sample (Fig. 40a) illustrates the relative uniformity of slip even more clearly. As evident from the figure, there are numerous closely spaced slip traces in the SC domains. The slip traces are more prominent in the cross-section since the component of the Burgers vector along the width of the sample is larger than the component along the thickness (Fig. 41). The images in Fig. 40 corresponds to one sample from each architecture but are representative of other samples.

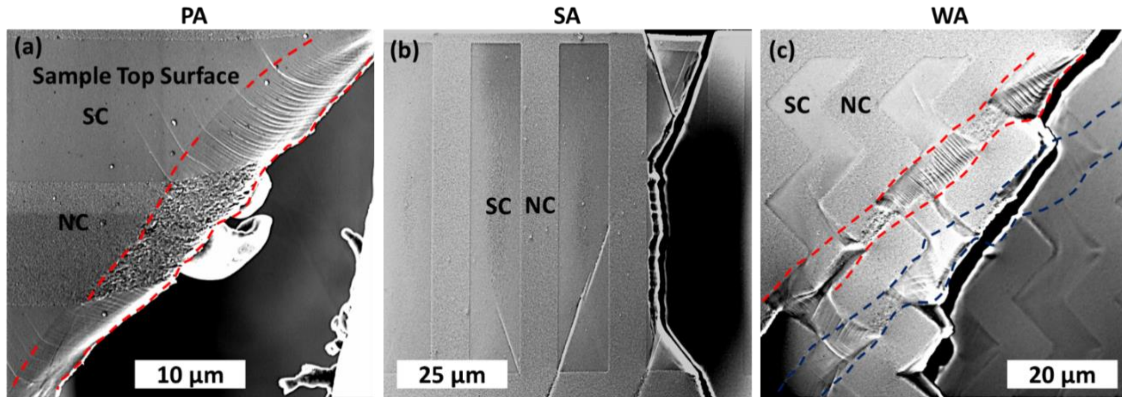

Figure 40: SEM micrographs of a fractured (a) PA, (b) SA and (c) WA sample. In the PA sample, the region outside the red dashed lines correspond to the sample top surface whereas the region within the red dashed lines correspond to the fracture surface. The SA sample fractured at an angle of 45° to the loading direction near the edge and perpendicular to the loading direction in the middle. The WA sample showed a tendency to localize slip along adjacent SC domains oriented in the same direction. Two sets of such SC domains are outlined in (c).

7.4 Discussions

The experimental results reported in this work reveal how the interplay between microstructural length scales and architecture influence the deformation and fracture behavior of bimodal Fe films. However, before analyzing the behavior of the bimodal films it is important to understand the behavior of the NC and SC domains that constitute these films. Therefore, the behavior of the pure NC and SC film is discussed first (Fig. 36a).

As evident from Fig. 36a, the NC film showed a high σ_y and a gradual elastic-plastic transition, which was followed by nearly perfect plastic behavior (no hardening) until failure. σ_y is high because of the extremely fine mean grain size, whereas the gradual elastic-plastic transition occurs due to inherently inhomogeneous nature of deformation at the nanoscale [95]. Similarly, the lack of strain hardening results from the inability of the NC grains to store dislocations, which typically originate

at a grain boundary, quickly traverse across the grain and get absorbed in the opposite grain boundary [6]. The absence of strain hardening leads to strain localization and early failure. It needs to be noted that all these characteristics are typical of NC metals in both bulk and thin film form and have been extensively documented [84,85].

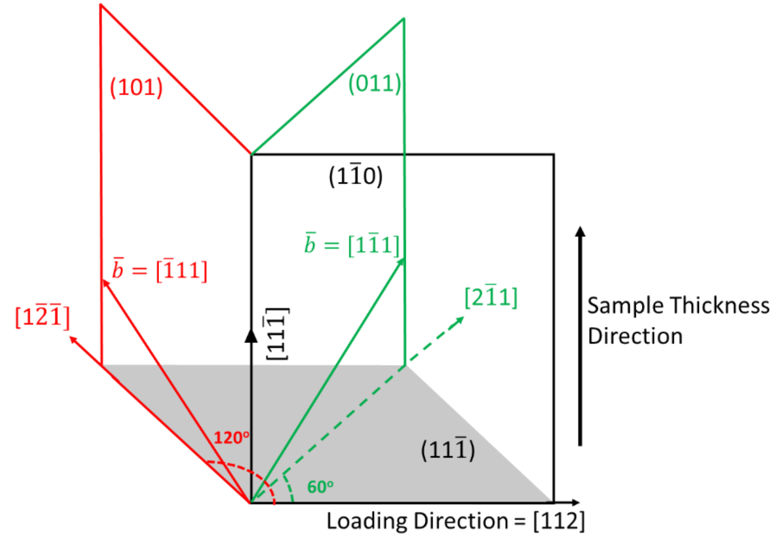

Figure 41: Schematic illustration of possible dislocation glide planes, (101) and (011), for SC Fe deformed along [112]. The Burgers vector of the dislocations in these planes are also shown.

Although the behavior of the pure NC film was similar to bulk NC metals, the behavior of the pure SC film was quite different from bulk SC samples. The SC film showed a high σ_y (850 MPa) and minimal ductility ($\varepsilon_f < 1\%$), which is exactly opposite to the behavior of bulk SC samples [96,97]. The high strength could possibly arise from sample size effects and the absence of defects in the as-fabricated samples [98]. However, the yield strength of the SC Fe films is still significantly higher than the strength exhibited by SC pillar specimens of comparable size under compression [99,100], which suggests a tension-compression asymmetry in yield strength of μm-sized SC Fe samples [101,102]. While the unusually high yield strength of the SC film is somewhat puzzling, the low ε_f can be explained through size effect phenomenon [103]. Once a dislocation source gets activated in the SC film, the nucleated dislocations escape to the surface and provide an easy glide path for

the following dislocations. Thus, it is difficult for the dislocations to interact, entangle and accumulate, which prevents work hardening and leads to strain localization and early failure.

Next, the behavior of the bimodal Fe film samples based on the deformation behavior of pure SC and NC samples was interpreted. The effect of SC and NC volume fraction on the behavior of PA samples is considered first. As mentioned earlier, σ_y of the PA samples increases with increasing NC volume fraction because of the co-deformation of the SC and NC domains. However, the strength of these samples is about 10% smaller compared to estimates using a simple rule of mixtures, which is surprising because bulk heterostructured metals with similar (lamellar) architecture show strengths higher than the predictions from a rule of mixtures [104].

This conundrum, however, can be explained as follows. When the PA samples are deformed, dislocation sources (e.g., single arm sources [105]) are first activated in the SC domains. Since the nucleated dislocations have a Burgers vector component along the width of the sample (Fig. 41), they are blocked at the interface with the NC domains and form pile-ups. The pile-ups lead to stress concentration at the SC/NC interface, which lead to the yielding of the NC domains at an applied stress smaller than their intrinsic yield strength. In effect, pile-ups in the SC domains weaken the NC domains and lead to a reduction in σ_y of the PA samples. Once the NC domains yield, strain localization occurs immediately because of the intrinsic lack of strain hardening capacity in the NC domains and the small volume of SC domains, which limits dislocation storage. As a result, ε_f is also quite low.

The same mechanism can also be used to explain the W_{SC} dependence of strength in all three architectures. In PA samples, as W_{SC} increases the number of dislocations that can be accommodated in the pile-up increases, and so does the stress concentration. Hence, yielding of NC domains occurs at progressively lower applied stress. Hence, PA1.3 sample has the lowest σ_y and PA1.1 sample has the highest σ_y (Fig. 37a). In the case of SA samples, the SC and NC domains do not co-deform and plasticity is confined to the SC domains, leading to the rupture of

the SC domains (Fig. 40b). Hence, their strength is independent of W_{SC} (Fig. 37b). However, plasticity is more uniformly distributed in the SC domains for small W_{SC}, which leads to relatively higher ε_f.

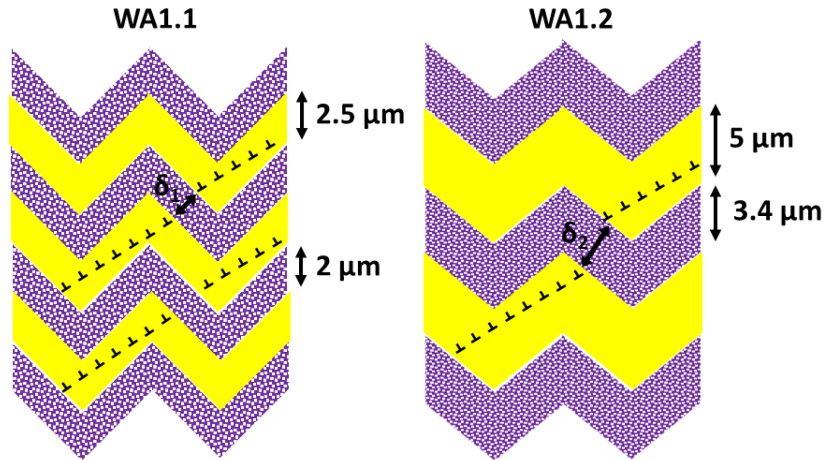

Figure 42: Schematic of dislocation pile-ups in WA samples with different W_{SC}. The number of dislocations in the pile-ups does not increase significantly with W_{SC} but the distance between the pile-ups (δ) does.

The WA samples present an interesting contrast to the PA samples wherein their σ_y increases with increasing W_{SC}. The reason for this behavior is as follows: Since the orientations of SC domains in the wave pattern (45° and 135° to the loading axis) are relatively close to the slip directions (oriented at 60° and 120°), the number of dislocations that can be accommodated in a pile-up does not significantly increase with an increase in W_{SC}. In other words, the stress concentration from individual pile-ups does not significantly increase with W_{SC}, as shown in Fig. 42. On the other hand, the interaction between stress fields arising from pile-ups in adjacent SC domains (inversely proportional to the distance between them) reduces because W_{NC} proportionally increases with W_{SC}. As a result, the combined stress field of the pile-ups become smaller, which lowers the stress concentration in the NC domains. Therefore, σ_y of the WA samples becomes larger with increasing W_{SC}.

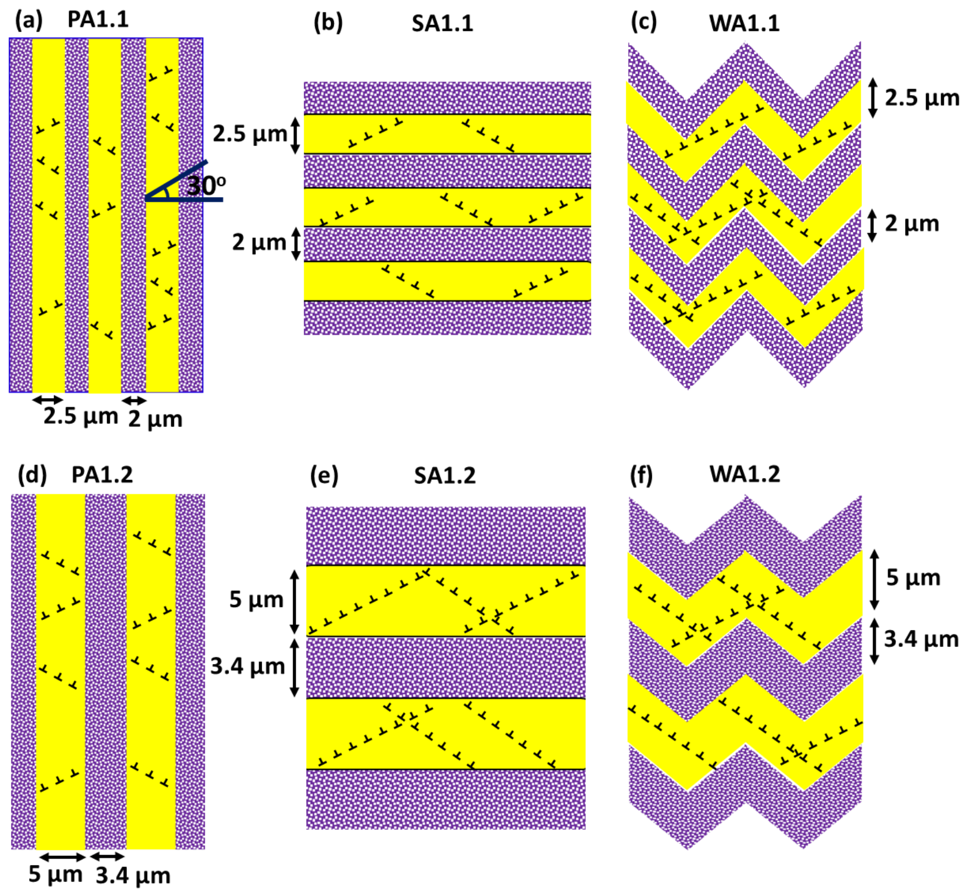

Figure 43: Schematic of dislocation pile-ups that occurs within SC domains of PA, SA, WA samples with different W_{SC}.

The above-described mechanism also explains the variations across different architectures for a given W_{SC} and constant volume fraction of SC and NC domains (section 3.2.3). As illustrated in Fig. 43, when W_{SC} = 2.5 µm the PA samples have the lowest stress concentration (smallest pile-ups) at the SC/NC interface and consequently the highest strength. At this W_{SC} the considerably larger pile-ups in the WA sample leads to much lower strength compared to both PA and SA samples. As W_{SC} increases, the pile-up length increases for both PA and SA samples while remaining relatively unchanged for WA samples. However, since the NC and SC domains co-deform only in the PA sample, a reduction in strength is seen only for those samples. Contrarily,

the greater separation between pile-ups in adjacent SC domains increases the strength of the WA samples. As a result, the WA sample becomes stronger than the PA sample at W_{SC} = 10 μm.

The experimental findings reported here highlight several important aspects of deformation in heterostructured metals. First and foremost, the strength-ductility synergy seen in bulk heterostructured metals does not translate to small sample length scales. Specifically, the bimodal Fe films show lower ε_f than the pure NC film, which is contrary to bulk behavior. This discrepancy arises because of the limited volume of the SC domains in the bimodal Fe films, which compromises their ability to store dislocations and strain harden. Nevertheless, if the thickness of the films is increased sufficiently (> 10 μm), the SC domains should recover their ability to accumulate dislocations and harden, which should lead to an increase in ε_f. As the film thickness increases, it should also lead to a decrease in strength of the SC domains, which will cause a reduction in the strength of the bimodal films. However, by carefully controlling the in-plane dimensions of the SC domains it may be possible to retain high strength while simultaneously extending the range of uniform macroscopic plastic deformation.

Secondly, the results emphasize the critical role of the microstructural architecture in determining the mechanical behavior of heterostructured metals. While a smaller W_{SC} increases σ_y of PA samples, it has the opposite effect in WA samples. Therefore, to optimize the mechanical properties of heterostructured metals, it is imperative to consider the collective effect of the microstructural length scales in the fine and coarse domains, the volume fractions of the domains as well as their spatial arrangement and connectivity. Finally, the results underscore the importance of the interplay between slip geometry and the spatial orientation of the coarse domains – a simplified mechanical model that ignores the geometry of dislocation slip would erroneously predict the highest σ_y for PA samples, which is clearly not the case.

Although the mechanisms depicted in Fig. 42 and 43 qualitatively account for the trends seen in σ_y for all three architectures, they cannot explain certain other aspects of deformation of the

bimodal Fe samples. For instance, it is not clear why the strength of SA samples matches or exceeds the strength of both PA and WA samples for all values of W_{SC}. Similarly, while both PA and WA samples exhibit shear failure (ductile fracture), SA samples rupture perpendicular to the loading direction in the middle of the film, which is indicative of brittle fracture. Computational simulations based on discrete dislocation dynamics [106,107] and crystal plasticity [108,109] could potentially resolve some of these questions and provide a fuller understanding of the deformation behavior of these films.

7.5 Conclusions

In this study, bimodal Fe films with three distinct architectures were synthesized using a novel method and their mechanical behavior was examined using MEMS testing stages. The experiments investigated the effect of three parameters – volume fraction of the NC and SC domains, width of the SC domains and the overall architecture – on the deformation behavior of the Fe films. The main conclusions are:

1. The strength of the bimodal Fe films is lower compared to the predictions from a simple rule-of-mixtures, which is contrary to the trend seen in bulk heterostructured metals.
2. The width of the SC domains has distinct effects on the behavior of the PA, SA and WA samples. Strength increases with decreasing W_{SC} for PA samples, whereas the opposite is true for WA samples. W_{SC} does not have a notable effect of the strength of SA samples. These contrasting trends emerge due to the interplay between the geometry of dislocation slip and the spatial orientation of the SC domains in the different architectures.
3. The PA samples have the highest strain to failure, irrespective of W_{SC}, since they require the SC and NC domains to co-deform. In the SA and WA samples strain localization leads to a small ε_f.

CHAPTER 8

CONCLUSIONS

8.1 Summary of Research Findings

This PhD dissertation focuses on the synthesis of metallic films with precisely controlled bimodal architectures and the effect of different microstructural architecture on the deformation behavior of the films. Here is the summary of the major research accomplishments and findings from this dissertation:

a) A novel method to synthesize the metallic films with bimodal architectures using Si substrate was developed. In this case, metallic films grew epitaxially on SC Si wafer whereas polycrystalline metallic film grew on SiN_x substrate. Using this method, heterostructured Cu and Fe films were synthesized and characterized using XRD, TEM and EBSD. This method enabled precise control of microstructural parameters like volume fraction of NC and SC domains and spatial arrangement and connectivity of NC and SC domains.

b) In the cases where metallic films could not grow epitaxially on SC Si, a different approach was designed to synthesize heterostructured metallic films. It can be viewed as an extension of the previous method. Here, a buffer layer was deposited on SC Si that enabled the epitaxial growth of other metals. This approach was demonstrated for two such systems, heterostructured Cr and heterostructured Ni. SC Ag and SC Fe was used as buffer layer for epitaxial growth of Ni and Cr respectively.

c) A new fabrication process was implemented to manufacture MEMS tensile testing stages along with the freestanding heterostructured Fe samples. The key accomplishments that resulted in the successful fabrication of the MEMS testing stages include reduction of residual stress in the heterostructured Fe sample, uniform etching of the samples and

redesign of the force-sensing beams to improve force resolution during tensile testing while simultaneously avoiding non-linearities.

d) Uniaxial tensile tests were performed on heterostructured Fe films with different bimodal architectures (PA – parallel architecture, SA – series architecture and WA – wave-like architecture) at quasi-static strain rate. The key findings from these experiments are: 1. The strength of bimodal Fe films is lower compared to simple rule-of-mixtures prediction. 2. The yield strength increased with decreasing single crystal width (W_{SC}) for PA samples, whereas the opposite was true for WA samples. 3. The effect of W_{SC} on the strength of SA samples was minimal. 4. In terms of strain to failure (ε_f), the PA samples showed the highest ε_f whereas in the SA and WA samples strain localization leads to a small ε_f.

8.2 Future Work

This dissertation research has demonstrated a method to synthesize heterostructured metallic films with precisely defined bimodal/multimodal architectures. Although the focus of this dissertation has been on understanding and tailoring the mechanical properties, the synthesis method could be used to tune other properties of thin films such as magnetic, electrical and shape memory. Likewise, there are several possibilities to extend the range of material systems that can be tailored using this method. Some of those possibilities are described below.

a) SC Si wafer was used as the main substrate for the epitaxial growth of metallic films. Other substrates like Al_2O_3, MgO, NaCl can be explored in future to generate a broader variety of heterostructured metallic films. In addition, non-metallic systems like ceramics might also be amenable for use with this method.

b) All the tensile testing experiments in this thesis were performed on Fe films with a thickness < 2 µm. While these experiments revealed several new insights on the deformation behavior of heterostructured Fe films with bimodal architectures, these insights may not translate to the bulk scale. For example, the SC domains can have significant strain

hardening in bulk samples since dislocations cannot easily escape to the surface. Therefore, it is necessary to study the effect of microstructural architectures on the mechanical properties of thicker heterostructured films to accurately predict the behavior of bulk heterostructured metals. Such a study would require synthesis of significantly thicker heterostructured films (20 -30 μm), redesign of MEMS device and modification of the tensile testing setup to account for the larger forces and displacements involved.

c) The heterostructured metal films in this work were synthesized with magnetron sputtering, which can utmost be used to create films that are tens of μm in thickness. In contrast, electrodeposition is a common, industrially relevant technique that can produce films/coating of much larger thickness. The heterostructured metallic films synthesized via sputtering can be used as a template for the growth of much thicker films (up to several mm) using electrodeposition.

d) The heterostructured metallic films can act as a template to grow 2D materials like h-BN, graphene, or even functional thin films like NiTi. 2D materials show range of interesting properties like high carrier mobilities, good thermal conductivity, superconductivity, high optical and UV adsorption. This method may provide a pathway to tune the properties of 2-D materials.

e) Although chapter 7 focused mainly on the three parameters mentioned above, the synthesis method enables a systematic investigation of a much broader set of parameters. For example, in addition to changing W_{SC} it is possible to vary the grain size in the polycrystalline domains by changing the deposition temperature. Using this approach, the microstructural length scale in both the fine and coarse domains can be controlled and systematically their interplay can be investigated. Another possibility is changing the loading direction to vary the number and type of active slip systems and studying their effect on different architectures. Finally, the film thickness can be increased to mitigate sample size effects, which will allow us to examine the intrinsic effects of each of these parameters.

REFERENCES

[1] B. Ravisankar, Equal-Channel Angular Pressing (ECAP), in: Handbook of Mechanical Nanostructuring, John Wiley & Sons, Ltd, 2015: pp. 277–297. https://doi.org/10.1002/9783527674947.ch13.

[2] K. Edalati, Z. Horita, A review on high-pressure torsion (HPT) from 1935 to 1988, Materials Science and Engineering: A. 652 (2016) 325–352. https://doi.org/10.1016/j.msea.2015.11.074.

[3] H. Halfa, Recent Trends in Producing Ultrafine Grained Steels, JMMCE. 02 (2014) 428–469. https://doi.org/10.4236/jmmce.2014.25047.

[4] Z.C. Cordero, B.E. Knight, C.A. Schuh, Six decades of the Hall–Petch effect – a survey of grain-size strengthening studies on pure metals, International Materials Reviews. 61 (2016) 495–512. https://doi.org/10.1080/09506608.2016.1191808.

[5] K.S. Kumar, H. Van Swygenhoven, S. Suresh, Mechanical behavior of nanocrystalline metals and alloys11The Golden Jubilee Issue—Selected topics in Materials Science and Engineering: Past, Present and Future, edited by S. Suresh, Acta Materialia. 51 (2003) 5743–5774. https://doi.org/10.1016/j.actamat.2003.08.032.

[6] Z. Budrovic, H.V. Swygenhoven, P.M. Derlet, S.V. Petegem, B. Schmitt, Plastic Deformation with Reversible Peak Broadening in Nanocrystalline Nickel, 304 (2004) 5.

[7] V. Yamakov, D. Wolf, S.R. Phillpot, A.K. Mukherjee, H. Gleiter, Dislocation processes in the deformation of nanocrystalline aluminium by molecular-dynamics simulation, Nature Mater. 1 (2002) 45–49. https://doi.org/10.1038/nmat700.

[8] R.C. Hugo, H. Kung, J.R. Weertman, R. Mitra, J.A. Knapp, D.M. Follstaedt, In-situ TEM tensile testing of DC magnetron sputtered and pulsed laser deposited Ni thin films, Acta Materialia. 51 (2003) 1937–1943. https://doi.org/10.1016/S1359-6454(02)00599-2.

[9] Y.H. Zhao, X.Z. Liao, S. Cheng, E. Ma, Y.T. Zhu, Simultaneously Increasing the Ductility and Strength of Nanostructured Alloys, Advanced Materials. 18 (2006) 2280–2283. https://doi.org/10.1002/adma.200600310.

[10] Y. Zhao, T. Topping, J.F. Bingert, J.J. Thornton, A.M. Dangelewicz, Y. Li, W. Liu, Y. Zhu, Y. Zhou, E.J. Lavernia, High Tensile Ductility and Strength in Bulk Nanostructured Nickel, Advanced Materials. 20 (2008) 3028–3033. https://doi.org/10.1002/adma.200800214.

[11] J. Li, Y. Cao, B. Gao, Y. Li, Y. Zhu, Superior strength and ductility of 316L stainless steel with heterogeneous lamella structure, J Mater Sci. 53 (2018) 10442–10456. https://doi.org/10.1007/s10853-018-2322-4.

[12] C.X. Huang, Y.F. Wang, X.L. Ma, S. Yin, H.W. Höppel, M. Göken, X.L. Wu, H.J. Gao, Y.T. Zhu, Interface affected zone for optimal strength and ductility in heterogeneous laminate, Materials Today. 21 (2018) 713–719. https://doi.org/10.1016/j.mattod.2018.03.006.

[13] T.H. Fang, W.L. Li, N.R. Tao, K. Lu, Revealing Extraordinary Intrinsic Tensile Plasticity in Gradient Nano-Grained Copper, Science. 331 (2011) 1587–1590. https://doi.org/10.1126/science.1200177.

[14] K. Lu, Making strong nanomaterials ductile with gradients, Science. 345 (2014) 1455–1456. https://doi.org/10.1126/science.1255940.

[15] D.B. Witkin, E.J. Lavernia, Synthesis and mechanical behavior of nanostructured materials via cryomilling, Progress in Materials Science. 51 (2006) 1–60. https://doi.org/10.1016/j.pmatsci.2005.04.004.

[16] F. Zhou, X.Z. Liao, Y.T. Zhu, S. Dallek, E.J. Lavernia, Microstructural evolution during recovery and recrystallization of a nanocrystalline Al-Mg alloy prepared by cryogenic ball milling, Acta Materialia. 51 (2003) 2777–2791. https://doi.org/10.1016/S1359-6454(03)00083-1.

[17] E.J. Lavernia, B.Q. Han, J.M. Schoenung, Cryomilled nanostructured materials: Processing and properties, Materials Science and Engineering: A. 493 (2008) 207–214. https://doi.org/10.1016/j.msea.2007.06.099.

[18] C. Sawangrat, S. Kato, D. Orlov, K. Ameyama, Harmonic-structured copper: performance and proof of fabrication concept based on severe plastic deformation of powders, J Mater Sci. 49 (2014) 6579–6585. https://doi.org/10.1007/s10853-014-8258-4.

[19] S. Billard, J.P. Fondère, B. Bacroix, G.F. Dirras, Macroscopic and microscopic aspects of the deformation and fracture mechanisms of ultrafine-grained aluminum processed by hot isostatic pressing, Acta Materialia. 54 (2006) 411–421. https://doi.org/10.1016/j.actamat.2005.09.012.

[20] X. Wu, F. Yuan, M. Yang, P. Jiang, C. Zhang, L. Chen, Y. Wei, E. Ma, Nanodomained Nickel Unite Nanocrystal Strength with Coarse-Grain Ductility, Scientific Reports. 5 (2015). https://doi.org/10.1038/srep11728.

[21] H. Gleiter, Nanocrystalline materials, Progress in Materials Science. 33 (1989) 223–315. https://doi.org/10.1016/0079-6425(89)90001-7.

[22] M.A. Meyers, A. Mishra, D.J. Benson, Mechanical properties of nanocrystalline materials, Progress in Materials Science. 51 (2006) 427–556. https://doi.org/10.1016/j.pmatsci.2005.08.003.

[23] C. Suryanarayana, Nanocrystalline materials, International Materials Reviews. 40 (1995) 41–64. https://doi.org/10.1179/imr.1995.40.2.41.

[24] H.V. Swygenhoven, P.M. Derlet, A. Hasnaoui, Atomistic Modeling of Strength of Nanocrystalline Metals, Advanced Engineering Materials. 5 (2003) 345–350. https://doi.org/10.1002/adem.200310080.

[25] C. Carlton, P.J. Ferreira, What is Behind the Inverse Hall-Petch Behavior in Nanocrystalline Materials?, MRS Online Proceedings Library (OPL). 976 (2006). https://doi.org/10.1557/PROC-976-0976-EE01-04.

[26] Z. Xie, Z. Wang, Y. Han, F. Han, Influence of Ge on crystallization kinetics, microstructure and high-temperature magnetic properties of Si-rich nanocrystalline FeAlSiBCuNbGe alloy, Journal of Non-Crystalline Solids. 463 (2017) 1–5. https://doi.org/10.1016/j.jnoncrysol.2017.02.015.

[27] E. Ma, Eight routes to improve the tensile ductility of bulk nanostructured metals and alloys, JOM. 58 (2006) 49–53. https://doi.org/10.1007/s11837-006-0215-5.

[28] Y. Zhao, Y. Zhu, E.J. Lavernia, Strategies for Improving Tensile Ductility of Bulk Nanostructured Materials, Advanced Engineering Materials. 12 (2010) 769–778. https://doi.org/10.1002/adem.200900335.

[29] P.G. Sanders, J.A. Eastman, J.R. Weertman, Elastic and tensile behavior of nanocrystalline copper and palladium, Acta Materialia. 45 (1997) 4019–4025. https://doi.org/10.1016/S1359-6454(97)00092-X.

[30] Y.H. Zhao, Q. Zhan, T.D. Topping, Y. Li, W. Liu, E.J. Lavernia, Improving ductility in ultrafine grained nickel with porosity and segregation via deformation, Materials Science and Engineering: A. 527 (2010) 1744–1750. https://doi.org/10.1016/j.msea.2009.10.064.

[31] E.W. Hart, Theory of the tensile test, Acta Metallurgica. 15 (1967) 351–355. https://doi.org/10.1016/0001-6160(67)90211-8.

[32] E. Ma, T. Zhu, Towards strength–ductility synergy through the design of heterogeneous nanostructures in metals, Materials Today. 20 (2017) 323–331. https://doi.org/10.1016/j.mattod.2017.02.003.

[33] M. Yang, Y. Pan, F. Yuan, Y. Zhu, X. Wu, Back stress strengthening and strain hardening in gradient structure, Materials Research Letters. 4 (2016) 145–151. https://doi.org/10.1080/21663831.2016.1153004.

[34] X.L. Wu, P. Jiang, L. Chen, J.F. Zhang, F.P. Yuan, Y.T. Zhu, Synergetic Strengthening by Gradient Structure, Materials Research Letters. 2 (2014) 185–191. https://doi.org/10.1080/21663831.2014.935821.

[35] Y. Wang, M. Chen, F. Zhou, E. Ma, High tensile ductility in a nanostructured metal, 419 (2002) 4.

[36] B.Q. Han, J. Ye, F. Tang, J. Schoenung, E.J. Lavernia, Processing and behavior of nanostructured metallic alloys and composites by cryomilling, J Mater Sci. 42 (2007) 1660–1672. https://doi.org/10.1007/s10853-006-0907-9.

[37] D. Witkin, Z. Lee, R. Rodriguez, S. Nutt, E. Lavernia, Al–Mg alloy engineered with bimodal grain size for high strength and increased ductility, Scripta Materialia. 49 (2003) 297–302. https://doi.org/10.1016/S1359-6462(03)00283-5.

[38] O. Ertorer, T. Topping, Y. Li, W. Moss, E.J. Lavernia, Enhanced tensile strength and high ductility in cryomilled commercially pure titanium, Scripta Materialia. 60 (2009) 586–589. https://doi.org/10.1016/j.scriptamat.2008.12.017.

[39] V.L. Tellkamp, E.J. Lavernia, A. Melmed, Mechanical behavior and microstructure of a thermally stable bulk nanostructured Al alloy, Metall Mater Trans A. 32 (2001) 2335–2343. https://doi.org/10.1007/s11661-001-0207-6.

[40] B.O. Han, E.J. Lavernia, Z. Lee, S. Nutt, D. Witkin, Deformation behavior of bimodal nanostructured 5083 Al alloys, Metall Mater Trans A. 36 (2005) 957–965. https://doi.org/10.1007/s11661-005-0289-7.

[41] Z. Lee, D.B. Witkin, V. Radmilovic, E.J. Lavernia, S.R. Nutt, Bimodal microstructure and deformation of cryomilled bulk nanocrystalline Al–7.5Mg alloy, Materials Science and Engineering: A. 410–411 (2005) 462–467. https://doi.org/10.1016/j.msea.2005.08.104.

[42] K. Lu, J. Lu, Nanostructured surface layer on metallic materials induced by surface mechanical attrition treatment, Materials Science and Engineering: A. 375–377 (2004) 38–45. https://doi.org/10.1016/j.msea.2003.10.261.

[43] W.L. Li, N.R. Tao, K. Lu, Fabrication of a gradient nano-micro-structured surface layer on bulk copper by means of a surface mechanical grinding treatment, Scripta Materialia. 59 (2008) 546–549. https://doi.org/10.1016/j.scriptamat.2008.05.003.

[44] X. Wu, M. Yang, F. Yuan, G. Wu, Y. Wei, X. Huang, Y. Zhu, Heterogeneous lamella structure unites ultrafine-grain strength with coarse-grain ductility, PNAS. 112 (2015) 14501–14505. https://doi.org/10.1073/pnas.1517193112.

[45] X. Wu, Y. Zhu, Heterogeneous materials: a new class of materials with unprecedented mechanical properties, Materials Research Letters. 5 (2017) 527–532. https://doi.org/10.1080/21663831.2017.1343208.

[46] R. Abdolvand, F. Ayazi, An advanced reactive ion etching process for very high aspect-ratio sub-micron wide trenches in silicon, Sensors and Actuators A: Physical. 144 (2008) 109–116. https://doi.org/10.1016/j.sna.2007.12.026.

[47] C.C. Koch, D.G. Morris, K. Lu, A. Inoue, Ductility of Nanostructured Materials, MRS Bull. 24 (1999) 54–58. https://doi.org/10.1557/S0883769400051551.

[48] G.D. Dutel, D. Tingaud, P. Langlois, G. Dirras, Nickel with multimodal grain size distribution achieved by SPS: microstructure and mechanical properties, J Mater Sci. 47 (2012) 7926–7931. https://doi.org/10.1007/s10853-012-6670-1.

[49] R. Thevamaran, O. Lawal, S. Yazdi, S.-J. Jeon, J.-H. Lee, E.L. Thomas, Dynamic creation and evolution of gradient nanostructure in single-crystal metallic microcubes, Science. 354 (2016) 312–316. https://doi.org/10.1126/science.aag1768.

[50] X. Wu, P. Jiang, L. Chen, F. Yuan, Y.T. Zhu, Extraordinary strain hardening by gradient structure, PNAS. 111 (2014) 7197–7201. https://doi.org/10.1073/pnas.1324069111.

[51] R. Sarkar, J. Rajagopalan, Synthesis of thin films with highly tailored microstructures, Materials Research Letters. 6 (2018) 398–405. https://doi.org/10.1080/21663831.2018.1471420.

[52] P.V. Liddicoat, X.-Z. Liao, Y. Zhao, Y. Zhu, M.Y. Murashkin, E.J. Lavernia, R.Z. Valiev, S.P. Ringer, Nanostructural hierarchy increases the strength of aluminium alloys, Nature Communications. 1 (2010) 63. https://doi.org/10.1038/ncomms1062.

[53] Y. Wei, Y. Li, L. Zhu, Y. Liu, X. Lei, G. Wang, Y. Wu, Z. Mi, J. Liu, H. Wang, H. Gao, Evading the strength–ductility trade-off dilemma in steel through gradient hierarchical nanotwins, Nature Communications. 5 (2014) 3580. https://doi.org/10.1038/ncomms4580.

[54] R. Valiev, Nanostructuring of metals by severe plastic deformation for advanced properties, Nature Materials. 3 (2004) 511–516. https://doi.org/10.1038/nmat1180.

[55] Q. Zhang, Y. Liu, Y. Liu, Y. Ren, Y. Wu, Z. Gao, X. Wu, P. Han, Enhanced tensile ductility and strength of electrodeposited ultrafine-grained nickel with a desired bimodal microstructure, Materials Science and Engineering: A. 701 (2017) 196–202. https://doi.org/10.1016/j.msea.2017.06.063.

[56] I. Petrov, P.B. Barna, L. Hultman, J.E. Greene, Microstructural evolution during film growth, J. Vac. Sci. Technol. A. 21 (2003) 13.

[57] H. Jiang, T.J. Klemmer, J.A. Barnard, E.A. Payzant, Epitaxial growth of Cu on Si by magnetron sputtering, Journal of Vacuum Science & Technology A. 16 (1998) 3376–3383. https://doi.org/10.1116/1.581489.

[58] R. Kawaguchi, T. Eguchi, S. Suto, Atomistic investigation on the initial stage of growth and interface formation of Fe on H-terminated Si(111)-(1 × 1) surface, Surface Science. 686 (2019) 52–57. https://doi.org/10.1016/j.susc.2019.04.002.

[59] C. Chang, J.C. Liu, J. Angilello, Epitaxy of (100) Cu on (100) Si by evaporation near room temperatures: In-plane epitaxial relation and channeling analysis, Appl. Phys. Lett. 57 (1990) 2239–2240. https://doi.org/10.1063/1.103902.

[60] C.M. Hull, J.A. Switzer, Electrodeposited Epitaxial Cu(100) on Si(100) and Lift-Off of Single Crystal-like Cu(100) Foils, ACS Appl. Mater. Interfaces. 10 (2018) 38596–38602. https://doi.org/10.1021/acsami.8b13188.

[61] I. Hashim, B. Park, H.A. Atwater, Epitaxial growth of Cu (001) on Si (001): Mechanisms of orientation development and defect morphology, Appl. Phys. Lett. 63 (1993) 2833–2835. https://doi.org/10.1063/1.110302.

[62] F. Cemin, D. Lundin, C. Furgeaud, A. Michel, G. Amiard, T. Minea, G. Abadias, Epitaxial growth of Cu(001) thin films onto Si(001) using a single-step HiPIMS process, Sci Rep. 7 (2017) 1655. https://doi.org/10.1038/s41598-017-01755-8.

[63] Y.-T. Cheng, Y.-L. Chen, W.-J. Meng, Y. Li, Formation of twins during epitaxial growth of α-iron films on silicon (111), Phys. Rev. B. 48 (1993) 14729–14732. https://doi.org/10.1103/PhysRevB.48.14729.

[64] S. Çörekçi, M.K. Öztürk, A. Bengi, M. Çakmak, S. Özçelik, E. Özbay, Characterization of an AlN buffer layer and a thick-GaN layer grown on sapphire substrate by MOCVD, J Mater Sci. 46 (2011) 1606–1612. https://doi.org/10.1007/s10853-010-4973-7.

[65] E.N. Jin, A.C. Lang, M.T. Hardy, N. Nepal, D.S. Katzer, D.F. Storm, B.P. Downey, D.J. Meyer, Epitaxial growth of $SrCaTiO_3$ films on GaN by molecular beam epitaxy with a TiO_2 buffer layer, Journal of Applied Physics. 127 (2020) 214104. https://doi.org/10.1063/5.0007144.

[66] L. Wang, X. Liu, Y. Zan, J. Wang, D. Wang, D. Lu, Z. Wang, Wurtzite GaN epitaxial growth on a Si(001) substrate using γ-Al2O3 as an intermediate layer, Appl. Phys. Lett. 72 (1998) 109–111. https://doi.org/10.1063/1.120660.

[67] Yu.N. Buzynin, Yu.N. Drozdov, M.N. Drozdov, A.Yu. Luk'yanov, O.I. Khrykin, A.N. Buzynin, A.E. Luk'yanov, E.I. Rau, F.A. Luk'yanov, Heteroepitaxial GaN films on silicon substrates with porous buffer layers, Bull. Russ. Acad. Sci. Phys. 72 (2008) 1499–1503. https://doi.org/10.3103/S1062873808110129.

[68] H. Zhang, Z. Ye, B. Zhao, Epitaxial growth of wurtzite GaN on Si(111) by a vacuum reactive evaporation, Journal of Applied Physics. 87 (2000) 2830–2834. https://doi.org/10.1063/1.372264.

[69] A.A. Ashra, A. Ueta, H. Kumano, I. Suemune, Role of ZnS bu!er layers in growth of zincblende ZnO on GaAs substrates by metalorganic molecular-beam epitaxy, Journal of Crystal Growth. (2000) 5.

[70] X.Q. Wang, H.P. Sun, X.Q. Pan, Effect of GaN interlayer on polarity control of epitaxial ZnO thin films grown by molecular beam epitaxy, Appl. Phys. Lett. 97 (2010) 151908. https://doi.org/10.1063/1.3502607.

[71] Z.D. Sha, J. Wang, Z.C. Chen, A.J. Chen, Z.Y. Zhou, X.M. Wu, L.J. Zhuge, Initial study on the structure and optical properties of ZnO film on Si(111) substrate with a SiC buffer layer, Physica E: Low-Dimensional Systems and Nanostructures. 33 (2006) 263–267. https://doi.org/10.1016/j.physe.2006.03.138.

[72] B. Pécz, A. El-Shaer, A. Bakin, A.-C. Mofor, A. Waag, J. Stoemenos, Structural characterization of ZnO films grown by molecular beam epitaxy on sapphire with MgO buffer, Journal of Applied Physics. 100 (2006) 103506. https://doi.org/10.1063/1.2382669.

[73] K.H. Westmacott, S. Hinderberger, U. Dahmen, Physical vapour deposition growth and transmission electron microscopy characterization of epitaxial thin metal films on single-crystal Si and Ge substrates, Philosophical Magazine A. 81 (2001) 1547–1578. https://doi.org/10.1080/01418610108214362.

[74] R. Abermann, Measurements of the intrinsic stress in thin metal films, Vacuum. 41 (1990) 1279–1282. https://doi.org/10.1016/0042-207X(90)93933-A.

[75] R. Abermann, R. Koch, The internal stress in thin silver, copper and gold films, Thin Solid Films. 129 (1985) 71–78. https://doi.org/10.1016/0040-6090(85)90096-3.

[76] R. Abermann, R. Kramer, J. Mäser, Structure and internal stress in ultra-thin silver films deposited on MgF2 and SiO substrates, Thin Solid Films. 52 (1978) 215–229. https://doi.org/10.1016/0040-6090(78)90140-2.

[77] R.W. Hoffman, Stresses in thin films: The relevance of grain boundaries and impurities, Thin Solid Films. 34 (1976) 185–190. https://doi.org/10.1016/0040-6090(76)90453-3.

[78] J.A. Alfonso, E.D. Greaves, B. Lavelle, L. Sajo-Bohus, Effect of sputtering pressure on residual stress in Ni films using energy-dispersive x-ray diffraction, Journal of Vacuum Science & Technology A. 21 (2003) 846–850. https://doi.org/10.1116/1.1575229.

[79] M. Ohring, Materials Science of Thin Films, Elsevier, 2001.

[80] F.M. D'Heurle, Aluminum films deposited by rf sputtering, Metall Mater Trans B. 1 (1970) 725–732. https://doi.org/10.1007/BF02811600.

[81] A.J. Ardell, Precipitation hardening, Metall Mater Trans A. 16 (1985) 2131–2165. https://doi.org/10.1007/BF02670416.

[82] P.J. Jacques, Transformation-induced plasticity for high strength formable steels, Current Opinion in Solid State and Materials Science. 8 (2004) 259–265. https://doi.org/10.1016/j.cossms.2004.09.006.

[83] V.M. Segal, Equal channel angular extrusion: from macromechanics to structure formation, Materials Science and Engineering: A. 271 (1999) 322–333. https://doi.org/10.1016/S0921-5093(99)00248-8.

[84] E. Ma, Instabilities and ductility of nanocrystalline and ultrafine-grained metals, Scripta Materialia. (2003) 6.

[85] Y.M. Wang, E. Ma, Strain hardening, strain rate sensitivity, and ductility of nanostructured metals, Materials Science and Engineering: A. 375–377 (2004) 46–52. https://doi.org/10.1016/j.msea.2003.10.214.

[86] Y. Zhao, T. Topping, J.F. Bingert, J.J. Thornton, A.M. Dangelewicz, Y. Li, W. Liu, Y. Zhu, Y. Zhou, E.J. Lavernia, High Tensile Ductility and Strength in Bulk Nanostructured Nickel, Adv. Mater. 20 (2008) 3028–3033. https://doi.org/10.1002/adma.200800214.

[87] J. Moering, X. Ma, J. Malkin, M. Yang, Y. Zhu, S. Mathaudhu, Synergetic strengthening far beyond rule of mixtures in gradient structured aluminum rod, Scripta Materialia. 122 (2016) 106–109. https://doi.org/10.1016/j.scriptamat.2016.05.006.

[88] Y.M. Wang, E. Ma, M.W. Chen, Enhanced tensile ductility and toughness in nanostructured Cu, Appl. Phys. Lett. 80 (2002) 2395–2397. https://doi.org/10.1063/1.1465528.

[89] D. Jia, Y.M. Wang, K.T. Ramesh, E. Ma, Y.T. Zhu, R.Z. Valiev, Deformation behavior and plastic instabilities of ultrafine-grained titanium, Appl. Phys. Lett. 79 (2001) 611–613. https://doi.org/10.1063/1.1384000.

[90] N. Rangaraju, T. Raghuram, B.V. Krishna, K.P. Rao, P. Venugopal, Effect of cryo-rolling and annealing on microstructure and properties of commercially pure aluminium, Materials Science and Engineering: A. 398 (2005) 246–251. https://doi.org/10.1016/j.msea.2005.03.026.

[91] R. Berlia, J. Rajagopalan, Synthesis of Heterostructured Metallic Films with Precisely Defined Multimodal Microstructures, ACS Appl. Mater. Interfaces. 13 (2021) 46097–46104. https://doi.org/10.1021/acsami.1c10999.

[92] H. Yilmaz, C.J. Williams, J. Risan, B. Derby, The size dependent strength of Fe, Nb and V micropillars at room and low temperature, Materialia. 7 (2019) 100424. https://doi.org/10.1016/j.mtla.2019.100424.

[93] R. Huang, Q.-J. Li, Z.-J. Wang, L. Huang, J. Li, E. Ma, Z.-W. Shan, Flow Stress in Submicron BCC Iron Single Crystals: Sample-size-dependent Strain-rate Sensitivity and Rate-dependent Size Strengthening, Materials Research Letters. 3 (2015) 121–127. https://doi.org/10.1080/21663831.2014.999953.

[94] P. Franciosi, L.T. Le, G. Monnet, C. Kahloun, M.-H. Chavanne, Investigation of slip system activity in iron at room temperature by SEM and AFM in-situ tensile and compression tests of iron single crystals, International Journal of Plasticity. 65 (2015) 226–249. https://doi.org/10.1016/j.ijplas.2014.09.008.

[95] G. Saada *, From the single crystal to the nanocrystal, Philosophical Magazine. 85 (2005) 3003–3018. https://doi.org/10.1080/14786430500154489.

[96] A.S. Keh, Y. Nakada, Plasticity of iron single crystals, Can. J. Phys. 45 (1967) 1101–1120. https://doi.org/10.1139/p67-081.

[97] W.A. Spitzig, A.S. Keh, The effect of orientation and temperature on the plastic flow properties of iron single crystals, Acta Metallurgica. 18 (1970) 611–622. https://doi.org/10.1016/0001-6160(70)90090-8.

[98] T.A. Parthasarathy, S.I. Rao, D.M. Dimiduk, M.D. Uchic, D.R. Trinkle, Contribution to size effect of yield strength from the stochastics of dislocation source lengths in finite samples, Scripta Materialia. 56 (2007) 313–316. https://doi.org/10.1016/j.scriptamat.2006.09.016.

[99] B.R.S. Rogne, C. Thaulow, Effect of crystal orientation on the strengthening of iron micro pillars, Materials Science and Engineering: A. 621 (2015) 133–142. https://doi.org/10.1016/j.msea.2014.10.067.

[100] B.R.S. Rogne, C. Thaulow, Strengthening mechanisms of iron micropillars, Philosophical Magazine. 95 (2015) 1814–1828. https://doi.org/10.1080/14786435.2014.984004.

[101] J.W. Christian, Some surprising features of the plastic deformation of body-centered cubic metals and alloys, Metall Mater Trans A. 14 (1983) 1237–1256. https://doi.org/10.1007/BF02664806.

[102] C.J. Healy, G.J. Ackland, Molecular dynamics simulations of compression–tension asymmetry in plasticity of Fe nanopillars, Acta Materialia. 70 (2014) 105–112. https://doi.org/10.1016/j.actamat.2014.02.021.

[103] J. Krebs, S.I. Rao, S. Verheyden, C. Miko, R. Goodall, W.A. Curtin, A. Mortensen, Cast aluminium single crystals cross the threshold from bulk to size-dependent stochastic plasticity, Nature Mater. 16 (2017) 730–736. https://doi.org/10.1038/nmat4911.

[104] X. Wu, M. Yang, F. Yuan, G. Wu, Y. Wei, X. Huang, Y. Zhu, Heterogeneous lamella structure unites ultrafine-grain strength with coarse-grain ductility, PNAS. 112 (2015) 14501–14505. https://doi.org/10.1073/pnas.1517193112.

[105] F. Mompiou, M. Legros, A. Sedlmayr, D.S. Gianola, D. Caillard, O. Kraft, Source-based strengthening of sub-micrometer Al fibers, Acta Materialia. 60 (2012) 977–983. https://doi.org/10.1016/j.actamat.2011.11.005.

[106] S. Akarapu, H.M. Zbib, D.F. Bahr, Analysis of heterogeneous deformation and dislocation dynamics in single crystal micropillars under compression, International Journal of Plasticity. 26 (2010) 239–257. https://doi.org/10.1016/j.ijplas.2009.06.005.

[107] G. Po, M.S. Mohamed, T. Crosby, C. Erel, A. El-Azab, N. Ghoniem, Recent Progress in Discrete Dislocation Dynamics and Its Applications to Micro Plasticity, JOM. 66 (2014) 2108–2120. https://doi.org/10.1007/s11837-014-1153-2.

[108] L. Li, P. Anderson, M. Lee, E. Bitzek, P. Derlet, H. Swygenhoven, The stress–strain response of nanocrystalline metals: A quantized crystal plasticity approach, Acta Materialia. 57 (2009) 812–822. https://doi.org/10.1016/j.actamat.2008.10.035.

[109] L. Li, M.-G. Lee, P.M. Anderson, Critical Strengths for Slip Events in Nanocrystalline Metals: Predictions of Quantized Crystal Plasticity Simulations, Metallurgical and Materials Transactions A. 42 (2011) 3875–3882. https://doi.org/10.1007/s11661-010-0392-2.